

# Wannier Functions Dually Localized in Space and Energy

Aaron Mahler

*Duke University, Department of Physics, Durham, NC 27708*

Jacob Z. Williams

*Duke University, Department of Chemistry, Durham, NC 27708*

Neil Qiang Su

*Department of Chemistry, Key Laboratory of Advanced Energy Materials Chemistry (Ministry of Education) and Renewable Energy Conversion and Storage Center (RECAST), Nankai University, Tianjin 300071, China and Duke University, Department of Chemistry, Durham, NC 27708*

Weitao Yang\*

*Duke University, Department of Chemistry, Durham, NC 27708 and*

*Duke University, Department of Physics, Durham, NC 27708*

(Dated: May 20, 2025)

The construction of Wannier functions from Bloch orbitals offers a unitary freedom that can be exploited to yield Wannier functions with advantageous properties. Minimizing the spatial variance is a well-known choice; another, previously proposed for Wannier functions constructed from the occupied Bloch manifold, minimizes a weighted sum of spatial and energy variance. Departing from all previous work, we extend dual localization to include both valence and conduction bands together. Near the Fermi energy, these dually localized Wannier functions yield frontier (bonding and antibonding) orbitals in bulk silicon and molecular ethylene, as well as  $d$ -orbital character in metallic copper. Because they are both localized and retain information about the orbital energy spectrum, dually localized Wannier functions are well suited to orbital-dependent methods that associate Wannier functions with specific energy ranges. They naturally induce fractional occupations, allowing for corrections to the DFA total energy.

## I. INTRODUCTION

Choosing an orbital basis is one of the first decisions that must be made in a single-particle electronic structure theory calculation. The eigenstates  $|\psi_i\rangle$  of the Hamiltonian are perhaps the most obvious choice, since they separate the ground and excited states, and their associated orbital energies  $\varepsilon_i$  are related to experimentally meaningful quantities like ionization potentials [1–4]. But they are not always convenient; for example, they may be spatially delocalized. This always occurs for periodic Hamiltonians, whose eigenstates are Bloch functions  $\psi_{\mathbf{k}i}(\mathbf{r}) = e^{i\mathbf{k}\cdot\mathbf{r}}u_{\mathbf{k}i}(\mathbf{r})$ , a plane wave multiplied by a function sharing the Hamiltonian’s periodicity [5]. Bloch functions’ delocalization limits their utility in describing spatially local properties like chemical bonds.

Wannier functions (WFs) [6], a localized, orthonormal basis set with the same translational symmetry as the Bloch orbitals, offer a compelling alternative. WFs were used to describe the electronic structure of crystals [7–9] long before there was a practical way to compute them [10]. Modern uses of Wannier functions rely on the gauge freedom, or unitary ambiguity, in their definition, which allows considerable flexibility in their construction. The standard implementation today is doubtless the maximally localized Wannier functions (MLWFs) of Marzari

and Vanderbilt [11]. MLWFs choose the gauge that minimizes a cost function measuring the WFs’ spatial variance; when constructed from the occupied bands of insulators with vanishing Chern numbers, MLWFs decay exponentially in three and fewer dimensions [7, 9, 12, 13]. MLWFs also see widespread use in electronic structure calculations; for example, evaluating dipole moments [14–16], as a basis set for large-scale simulations [17–20], interpolating band structures [21], and as a picture of chemical bonding [11, 22]. Localized orbitals are necessary for corrections to delocalization error in density functional theory [23, 24], and MLWFs are a well-studied choice [25–29].

Despite their many successes, however, maximally localized Wannier functions cannot serve as a complete basis for single-particle orbitals. Part of the process for doing calculations with MLWFs is choosing the bands from which they are constructed; in the case of semiconductors, this is often the valence manifold. If more bands are included in the MLWFs’ construction, they will become more localized (since the Bloch functions are a complete basis). In the limit at which all conduction bands are included, MLWFs tend to a comb of delta functions, which are no longer useful for calculations. The recent projectability disentanglement [30] and automated mixing [31] methods allow MLWFs to be constructed automatically with admixture from low-energy conduction bands, but they still cannot be used as a complete basis. Gygi *et al.* [32] proposed adding energy variance to the MLWF cost function; this alternate gauge, described as

\* weitao.yang@duke.edu

mixed Wannier–Bloch functions, was implemented for valence bands by Giustino and Pasquarello [33].

In this work, we extend the mixed spatial–energy localization gauge to the full space of valence and conduction bands. In this context, we call the localized orbitals dually localized Wannier functions (DLWFs). DLWFs have three unique features. First, the addition of energy localization makes DLWFs a complete basis for single-particle states: they can be constructed freely from any number of valence and conduction bands. Second, mixing the valence and conduction manifolds yields DLWFs with fractional occupations. These induce changes  $\Delta E$  to the total energy in methods to correct delocalization error in density functional theory, such as the localized orbital scaling correction (LOSC) [34–36] and the Koopmans-compliant Wannier (KCW) functional [24, 29]. A nonzero  $\Delta E$  is critical for describing the breaking of molecular chemical bonds and in describing large, ionized molecules [34]; therefore, it is also necessary for the consistent description of bulk–molecule interfaces. Third, DLWFs whose energy is localized near the Fermi level appear as localized frontier orbitals, capturing both bonding and antibonding character in silicon and ethylene as well as orbitals resembling the  $d$  manifold in copper. They extend the frontier molecular orbital paradigm [37] to materials, a necessary step toward simulating chemical reactivity at interfaces. DLWFs thus promise broad application to simulating electronic structure and chemical reactions of both materials and interfaces.

## II. THEORY

We will assume a Monkhorst–Pack mesh [38], in which a uniform grid of  $N_k$   $\mathbf{k}$ -points (including the origin  $\Gamma$ ) in the first Brillouin zone define the Bloch orbitals, throughout. Under this assumption, Wannier functions take the form

$$|w_{\mathbf{R}i}\rangle = \frac{1}{N_k} \sum_{\mathbf{k}} e^{-i\mathbf{k}\cdot\mathbf{R}} |\psi_{\mathbf{k}i}\rangle, \quad (1)$$

where  $\mathbf{R}$  indexes unit cells in the unfolded supercell on which the Wannier functions are periodic (following Born–von Kàrmàn boundary conditions [5]). This normalization convention implies that  $\langle\psi_{\mathbf{k}i}|\psi_{\mathbf{q}j}\rangle = N_k\delta_{ij}\delta_{\mathbf{k}\mathbf{q}}$  and that  $|\psi_{\mathbf{k}i}\rangle = \sum_{\mathbf{R}} e^{i\mathbf{k}\cdot\mathbf{R}} |w_{\mathbf{R}i}\rangle$ . For simplicity of notation, we omit the spin index, but our arguments apply independently to each spin channel of a collinear spin-polarized system.

### A. Gauge freedom

At each  $\mathbf{k}$ , Bloch orbitals are defined only up to a global phase  $e^{i\theta_{\mathbf{k}n}}$ . This yields a gauge freedom when constructing a Wannier functions from a single band,

since

$$|w_{\mathbf{R}i}\rangle = \frac{1}{N_k} \sum_{\mathbf{k}} e^{-i\mathbf{k}\cdot\mathbf{R}} e^{i\theta_{\mathbf{k}i}} |\psi_{\mathbf{k}i}\rangle. \quad (2)$$

To construct localized WFs,  $\theta_i(\mathbf{k})$  should be chosen such that  $e^{i\theta_i(\mathbf{k})}\psi_i(\mathbf{k})$  is as smooth as possible; if it is analytic, the resulting Wannier function is exponentially localized [9]. When Wannier functions are constructed from multiple bands, the gauge freedom expands to include any unitary combination  $U^{\mathbf{k}}$  of the bands at the same  $\mathbf{k}$ -point [8]. (These are formally called *generalized* Wannier functions, but we will refer to them as Wannier functions throughout the text.) Thus

$$\begin{aligned} |w_{\mathbf{R}i}\rangle &= \frac{1}{N_k} \sum_{\mathbf{k}} e^{-i\mathbf{k}\cdot\mathbf{R}} \sum_j U_{ji}^{\mathbf{k}} |\psi_{\mathbf{k}j}\rangle \\ &= \frac{1}{N_k} \sum_{\mathbf{k}} e^{-i\mathbf{k}\cdot\mathbf{R}} |\phi_{\mathbf{k}i}\rangle. \end{aligned} \quad (3)$$

We call the intermediate  $|\phi_{\mathbf{k}i}\rangle = \sum_j U_{ji}^{\mathbf{k}} |\psi_{\mathbf{k}j}\rangle$  transformed Bloch orbitals.

### B. Cost functions

It is the unitary gauges  $U^{\mathbf{k}}$  that give Wannier functions their practical flexibility. Maximally localized Wannier functions [11] choose  $U^{\mathbf{k}}$  that minimize the cost function

$$\Omega = \sum_i \langle w_{\mathbf{0}i} | \Delta r^2 | w_{\mathbf{0}i} \rangle; \quad (4)$$

that is, the sum of each MLWF’s spatial variance

$$\langle w_{\mathbf{0}i} | \Delta r^2 | w_{\mathbf{0}i} \rangle = \langle w_{\mathbf{0}i} | r^2 | w_{\mathbf{0}i} \rangle - |\langle w_{\mathbf{0}i} | \mathbf{r} | w_{\mathbf{0}i} \rangle|^2, \quad (5)$$

integrated over the supercell. Eq. (4) is the natural extension to periodic boundary conditions of Foster–Boys localization for finite systems [39]. Without loss of generality, only the home unit cell  $\mathbf{R} = \mathbf{0}$  is included in the cost function because Wannier functions at  $\mathbf{R}$  are related by translation to those at  $\mathbf{0}$ ,  $w_{\mathbf{R}i}(\mathbf{r}) = w_{\mathbf{0}i}(\mathbf{r} - \mathbf{R})$ . Summing over  $\mathbf{R}$  would thus change  $\Omega$  only by a multiplicative constant. The MLWF formulation was originally applied to a *composite* set of Bloch bands, separated by an energy gap from all other states at every point in the Brillouin zone. The gradient of  $\Omega$  was derived analytically for a composite set by Marzari and Vanderbilt [11], and descent methods are applied to obtain the  $U^{\mathbf{k}}$  which minimize  $\Omega$ .

Gygi *et al.* [32] proposed adding an energy variance term to  $\Omega$ , yielding the dual-localization cost function

$$\begin{aligned} F &:= (1 - \gamma)\Omega + C\gamma\Xi \\ &= (1 - \gamma) \sum_i \langle w_{\mathbf{0}} | \Delta r^2 | w_{\mathbf{0}i} \rangle \\ &\quad + C\gamma \sum_i \langle w_{\mathbf{0}i} | \Delta h^2 | w_{\mathbf{0}i} \rangle. \end{aligned} \quad (6)$$

Here,  $h$  is the single-particle Hamiltonian,  $\Omega$  the spatial spread, and  $\Xi$  the energy spread;

$$\langle w_{\mathbf{0}i} | \Delta h^2 | w_{\mathbf{0}i} \rangle = \langle w_{\mathbf{0}i} | h^2 | w_{\mathbf{0}i} \rangle - |\langle w_{\mathbf{0}i} | h | w_{\mathbf{0}i} \rangle|^2 \quad (7)$$

is the energy variance of  $|w_{\mathbf{0}i}\rangle$ ; and the unitful constant  $C = 1 \text{ \AA}^2/\text{eV}^2$  restores dimensional consistency of  $F$  [40]. The mixing term  $\gamma \in [0, 1]$  can be tuned to prioritize spatial or energy localization (see Sec. II E).

Our work extends [32] and [33], which uses  $F$  to construct electrons and phonon WFs in bulk systems, in two ways. First, [32, 33] apply only to calculations in which the Brillouin zone is sampled only at the origin  $\Gamma$  of reciprocal space. In this case, the transformed Bloch orbitals are equivalent to the Wannier functions; varying the mixing term  $\gamma$  interpolates between MLWFs (at  $\gamma = 0$ ) and Bloch orbitals ( $\gamma = 1$ ), so the resulting  $|w_{\mathbf{R}i}\rangle$  are called Wannier–Bloch functions. When  $N_k > 1$ , a nontrivial discrete Fourier transform is required to map  $|\phi_{\mathbf{k}i}\rangle$  to  $|w_{\mathbf{R}i}\rangle$ , and the Wannier functions do not reduce to the Bloch orbitals at  $\gamma = 1$ ; in this case, we call the WFs minimizing  $F$  dually localized Wannier functions. Second, Wannier–Bloch functions are constructed from only the occupied (valence) Bloch manifold. We show that  $F$  allows Wannier functions to be built from both valence and conduction bands at once, treating both on the same footing.

### 1. Minimizing the cost function

Marzari and Vanderbilt [11] minimize  $\Omega$  for a composite set of energy bands by determining its gradient with respect to  $U^{\mathbf{k}}$ . This is accomplished by splitting the cost function into two positive definite quantities,  $\Omega = \Omega_I + \tilde{\Omega}$ .  $\Omega_I$  is invariant to the choice of gauge, so minimizing  $\Omega$  is equivalent to minimizing only the gauge-dependent term  $\tilde{\Omega}$ . For a set of  $N_w$  Wannier functions,

$$\Omega_I = \sum_i^{N_w} \left( \langle w_{\mathbf{0}i} | r^2 | w_{\mathbf{0}i} \rangle - \sum_j^{N_w} \sum_{\mathbf{R}}^{N_k} |\langle w_{\mathbf{R}j} | \mathbf{r} | w_{\mathbf{0}i} \rangle|^2 \right), \quad (8)$$

and the gauge-dependent spatial cost is

$$\tilde{\Omega} = \sum_{j \neq i}^{N_w} \sum_{\mathbf{R}}^{N_k} |\langle w_{\mathbf{R}j} | \mathbf{r} | w_{\mathbf{0}i} \rangle|^2 + \sum_i^{N_w} \sum_{\mathbf{R} \neq \mathbf{0}}^{N_k} |\langle w_{\mathbf{R}i} | \mathbf{r} | w_{\mathbf{0}i} \rangle|^2. \quad (9)$$

By an argument exactly analogous to that in [11], the energy cost  $\Xi$  splits into a gauge-invariant term  $\Xi_I$  and

the gauge-dependent  $\tilde{\Xi}$ ,

$$\begin{aligned} \Xi &= \Xi_I + \tilde{\Xi} \\ &= \sum_i \left( \langle w_{\mathbf{0}i} | h^2 | w_{\mathbf{0}i} \rangle - \sum_{\mathbf{R}j} |\langle w_{\mathbf{R}j} | h | w_{\mathbf{0}i} \rangle|^2 \right) \\ &\quad + \sum_i \sum_{\mathbf{R}j \neq \mathbf{0}i} |\langle w_{\mathbf{R}j} | h | w_{\mathbf{0}i} \rangle|^2. \end{aligned} \quad (10)$$

Thus, for a composite set of bands, we find the unitary operators  $U^{\mathbf{k}}$  defining the DLWF gauge by minimizing

$$\tilde{F} = (1 - \gamma)\tilde{\Omega} + C\gamma\tilde{\Xi}. \quad (11)$$

Because differentiation is linear, the gradients of  $\tilde{\Omega}$  and  $\tilde{\Xi}$  with respect to  $U^{\mathbf{k}}$  can be found in parallel, and the minimum found with an iterative procedure. Virtual Bloch bands almost never form a composite set, however, so we require an additional step to construct DLWFs.

### C. Disentanglement

The valence bands of metals, and the conduction bands of most systems, cannot be separated from the rest of the bands by an energy gap everywhere in the Brillouin zone; such bands are said to be *entangled*. Souza et al. developed a *disentanglement* method, extracting a subset of interest from a set of entangled bands [21]. From  $N_b$  Bloch bands, which we now index with  $n$ , disentanglement obtains  $N_w \leq N_b$  composite bands that are as smooth as possible in  $\mathbf{k}$ ; this turns out to be accomplished by minimizing  $\Omega_I$  iteratively. We write  $|\tilde{\psi}_{\mathbf{k}i}\rangle$ , with  $1 \leq i \leq N_w$ , for the disentangled bands; they are obtained as

$$|\tilde{\psi}_{\mathbf{k}i}\rangle = \sum_n V_{in}^{\mathbf{k}} |\psi_{\mathbf{k}n}\rangle. \quad (12)$$

Here,  $V^{\mathbf{k}}$  is a  $N_w \times N_b$  semiunitary transformation that satisfies  $V^{\mathbf{k}}(V^{\mathbf{k}})^\dagger = \mathbb{1}$ , the  $N_w$ -dimensional identity operator. Applying  $U^{\mathbf{k}}$  to  $|\tilde{\psi}_{\mathbf{k}i}\rangle$  generates the transformed Bloch orbitals  $|\phi_{\mathbf{k}i}\rangle$ , which are Fourier transformed to generate  $|w_{\mathbf{R}i}\rangle$ . The combined disentanglement, localization, and Wannierization process is

$$\begin{aligned} w_{\mathbf{R}i}(\mathbf{r}) &= \frac{1}{N_k} \sum_{\mathbf{k}}^{N_k} e^{-i\mathbf{k} \cdot \mathbf{R}} \phi_{\mathbf{k}i}(\mathbf{r}) \\ &= \frac{1}{N_k} \sum_{\mathbf{k}}^{N_k} e^{-i\mathbf{k} \cdot \mathbf{R}} \sum_j^{N_w} U_{ij}^{\mathbf{k}} \tilde{\psi}_{\mathbf{k}j}(\mathbf{r}) \\ &= \frac{1}{N_k} \sum_{\mathbf{k}}^{N_k} e^{-i\mathbf{k} \cdot \mathbf{R}} \sum_j^{N_w} U_{ij}^{\mathbf{k}} \sum_n^{N_b} V_{jn}^{\mathbf{k}} \psi_{\mathbf{k}n}(\mathbf{r}). \end{aligned} \quad (13)$$

In principle, we could modify the disentanglement procedure in the same way that  $F$  modifies  $\Omega$ , finding the  $N_w$ -dimensional subspace that minimizes

$$F_I = (1 - \gamma)\Omega_I + \gamma\Xi_I. \quad (14)$$

In practice, however, we find this unnecessary; we use the space-only disentanglement of [21] as the first step in computing the DLWFs. In particular, this procedure projects the Hamiltonian onto the subspace spanned by  $\{|\psi_{\mathbf{k}i}\rangle\}$  after each iteration, yielding a disentangled Hamiltonian  $\tilde{h} = \sum_{\mathbf{k}} V^{\mathbf{k}} h (V^{\mathbf{k}})^{\dagger}$  that satisfies

$$\langle \tilde{\psi}_{\mathbf{k}i} | \tilde{h} | \tilde{\psi}_{\mathbf{q}j} \rangle = N_k \delta_{\mathbf{k}\mathbf{q}} \delta_{ij} \tilde{\varepsilon}_{\mathbf{k}i}, \quad (15)$$

where  $\tilde{\varepsilon}_{\mathbf{k}i}$  is a disentangled energy eigenvalue. (If we modify  $\Xi$  to use the disentangled Hamiltonian, then  $\Xi_I = 0$  trivially. See the Supplemental Material [41] for the derivation.)

The difference between the original and disentangled Hamiltonian depends on the subspace projectors  $V^{\mathbf{k}}$ . If every disentangled eigenvalue  $\tilde{\varepsilon}_{\mathbf{k}i}$  corresponds exactly to a Bloch eigenvalue  $\varepsilon_{\mathbf{k}n}$  at the same  $\mathbf{k}$ -point, then  $h$  and  $\tilde{h}$  commute inside the disentangled subspace and using  $\tilde{h}$  is equivalent to using  $h$  in  $\Xi$ . We do not achieve this in practice, but the existing disentanglement procedure creates a band structure nearly equivalent to the full band structure except for high-energy conduction bands. We can thus reproduce the band structure around the Fermi energy accurately by including sufficiently many unoccupied orbitals before disentanglement; the band structure interpolated from the resulting Wannier functions differs appreciably from the original only well above the Fermi energy. For example, a band structure for silicon disentangling 34 bands to 30 yields DLWFs that interpolate a qualitatively accurate band structure up to 20 eV above the Fermi energy (Fig. 1).

Replacing  $h$  by the disentangled Hamiltonian  $\tilde{h}$  also means that  $\sum_i \langle w_{\mathbf{0}i} | \tilde{h}^2 | w_{\mathbf{0}i} \rangle$  is gauge-invariant, since

$$\sum_i^{N_w} \langle w_{\mathbf{0}i} | \tilde{h}^2 | w_{\mathbf{0}i} \rangle = \frac{1}{N_k} \text{Tr} \left[ (\tilde{h})^2 \right]. \quad (16)$$

We thus decompose

$$\begin{aligned} \Xi &= \sum_i \left[ \langle w_{\mathbf{0}i} | \tilde{h}^2 | w_{\mathbf{0}i} \rangle - |\langle w_{\mathbf{0}i} | \tilde{h} | w_{\mathbf{0}i} \rangle|^2 \right] \\ &:= \Xi_{\text{SA}} - \Xi_{\text{AS}}, \end{aligned} \quad (17)$$

where the squared average energy term  $\Xi_{\text{SA}}$  is invariant to the choice of Wannier basis. As is true for  $\Omega$  in  $\Gamma$ -sampled systems, minimizing  $\Xi$  (or  $\tilde{\Xi}$ ) is equivalent to maximizing the average energy squared term  $\Xi_{\text{AS}}$ .

#### D. Energy cost gradient

We now derive the gradient of  $\Xi_{\text{AS}}$  with respect to the localization unitary  $U^{\mathbf{k}}$ . To first order,  $U^{\mathbf{k}}$  can be written as a small anti-Hermitian perturbation to the identity;  $U^{\mathbf{k}} \approx 1 + W^{\mathbf{k}}$ , with  $(W^{\mathbf{k}})^{\dagger} = -W^{\mathbf{k}}$ . Then  $\partial \Xi_{\text{AS}} / \partial U^{\mathbf{k}}$  is obtained via the matrix calculus identity

$$\frac{d \text{Re Tr} [MW]}{dW} = \frac{1}{2} (M - M^{\dagger}) := \mathcal{A}[M]. \quad (18)$$

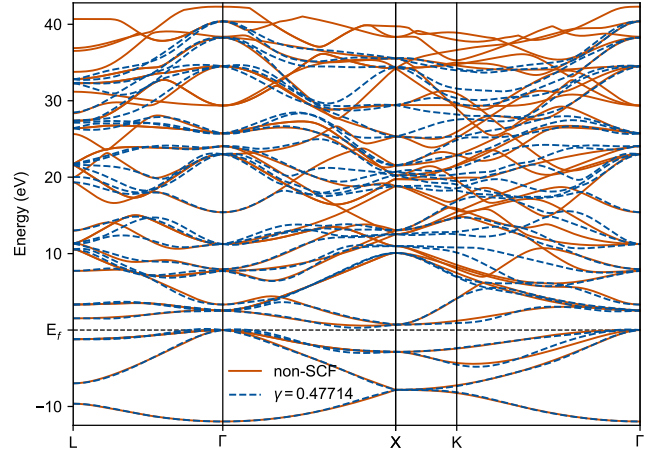


FIG. 1. PBE band structure of silicon (valence band maximum set to zero), disentangling 34 bands to 30 Wannier functions, with disentangled states below the Fermi energy fixed to reproduce the Bloch bands exactly. Solid orange bands are non-self-consistently computed in **Quantum ESPRESSO**; dashed blue bands are interpolated from the DLWFs. Mixing parameter  $\gamma = 0.47714$ .

To see why this is useful, observe that we may write

$$\begin{aligned} \Xi_{\text{AS}} &= \sum_i \left| \langle w_{\mathbf{0}i} | \tilde{h} | w_{\mathbf{0}i} \rangle \right|^2 = \sum_i \left| \frac{1}{N_k} \sum_{\mathbf{k}j} |U_{ij}^{\mathbf{k}}|^2 \tilde{\varepsilon}_{\mathbf{k}j} \right|^2 \\ &= \sum_i \left| \frac{1}{N_k} \sum_{\mathbf{k}} B_{ii}^{\mathbf{k}} \right|^2, \end{aligned} \quad (19)$$

where  $B_{ij}^{\mathbf{k}} = (U^{\mathbf{k}} \tilde{h} (U^{\mathbf{k}})^{\dagger})_{ij}$  is the Hamiltonian in the transformed Bloch basis. The change in  $\Xi_{\text{AS}}$  to first order in  $W^{\mathbf{k}}$  is then

$$\begin{aligned} d\Xi_{\text{AS}} &= \frac{4}{N_k^2} \sum_i \left( \sum_{\mathbf{k}} \text{Re} (B^{\mathbf{k}} W^{\mathbf{k}})_{ii} \right) \left( \sum_{\mathbf{k}'} B_{ii}^{\mathbf{k}'} \right) \\ &= \frac{4}{N_k^2} \sum_{\mathbf{k}\mathbf{k}'} \text{Re Tr} [C^{(\mathbf{k},\mathbf{k}')} W^{\mathbf{k}}], \end{aligned} \quad (20)$$

where  $(C^{(\mathbf{k},\mathbf{k}')} )_{ij} = B_{ji}^{\mathbf{k}} B_{jj}^{\mathbf{k}'}$ . We can thus write the gradient in terms of the superoperator  $\mathcal{A}$ , defined in Eq. (18), as

$$\begin{aligned} \frac{d\Xi_{\text{AS}}}{dW^{\mathbf{k}}} &= \frac{4}{N_k} \sum_{\mathbf{k}'} \mathcal{A} [C^{(\mathbf{k},\mathbf{k}')} ] \\ &= \frac{2}{N_k} \sum_{\mathbf{k}'} \left[ C^{(\mathbf{k},\mathbf{k}')} - (C^{(\mathbf{k},\mathbf{k}')} )^{\dagger} \right]. \end{aligned} \quad (21)$$

In this form, it appears the gradient  $\mathbf{k}$ -point depends on every other  $\mathbf{k}$ -point in the Brillouin zone. However, we can sum  $C^{(\mathbf{k},\mathbf{k}')}$  over  $\mathbf{k}'$  prior to evaluating the gradient. Thus

$$\left[ \frac{d\Xi_{\text{AS}}}{dW^{\mathbf{k}}} \right]_{ij} = 2B_{ij}^{\mathbf{k}} \left( \langle w_{\mathbf{0}j} | \tilde{h} | w_{\mathbf{0}j} \rangle - \langle w_{\mathbf{0}i} | \tilde{h} | w_{\mathbf{0}i} \rangle \right). \quad (22)$$



Thus,  $\Xi$  essentially penalizes mixing of each pair of Bloch orbitals in proportion to the difference in average energy between the Wannier functions they are used to construct. Eq. (22) also makes clear that the computational cost of computing  $d\Xi_{\text{AS}}/dW^{\mathbf{k}}$  is independent of  $N_k$ , so the overall cost of energy localization is linear in  $N_k$ .

### E. Space-energy mixing parameter

DLWFs are defined by the choice of the mixing parameter  $\gamma$  in Eq. (6). Setting  $\gamma = 0$  recovers the MLWF cost function  $\Omega$ . The Bloch orbitals are recovered at  $\gamma = 1$  if the Brillouin zone is sampled only at  $\Gamma$ ; when  $N_k > 1$ , setting  $\gamma = 1$  yields transformed Bloch orbitals  $|\phi_{\mathbf{k}n}\rangle$  equivalent to the original Bloch orbitals, ordered by their energy at each  $\mathbf{k}$ . If there are band crossings in the Brillouin zone, the energy-ordered Bloch orbitals will not be smooth in  $\mathbf{k}$ , giving poor spatial localization. Choosing  $\gamma$  strictly between 0 and 1, then, provides Wannier functions at least somewhat localized in both space and energy.

Unless specified otherwise, we set  $\gamma = 0.47714$ . This is equivalent, for lengths in Å and energies in eV, to that used in the LOSC method [35]. In that work,  $\gamma$  was chosen to minimize delocalization error on a suite of molecules. At this value of  $\gamma$ , we find that Bloch orbitals mix substantially only when their energies at a  $\mathbf{k}$ -point are within about 2 eV. This natural penalty to mixing of orbitals widely separated in energy means that dual localization yields converged frontier orbitals irrespective of the number of high-energy virtual states included. Details about the unit dependence of  $\gamma$  may be found in the Supplemental Material.

While  $\gamma = 0.47714$  has been an effective choice in a variety of applications in molecules as well as LOSC for materials (see Sec. IV), it does not satisfy a physical rule such as a variational principle. This is a blessing and a curse; it provides a parameter than can be tuned for the application of choice, but the character of the DLWFs (especially the occupied DLWFs, see Fig. 2) depends on  $\gamma$ .

### F. Implementation details

We implement the DLWF localization in a locally maintained fork [42] of the open-source **wannier90** code [43–45]. Following Marzari and Vanderbilt [11] for  $\Omega$  and the previous section for  $\Xi$ , we compute  $\partial F/\partial U^{\mathbf{k}}$  at each  $\mathbf{k}$ -point. Given an initial guess or disentanglement, either a conjugate gradient or steepest descent algorithm is used to minimize  $F$ . Some modifications to the conjugate gradient algorithm were required for  $\Xi$ , since we found that the step size that produced the best localization was system-dependent. To account for this, we sweep a range of step sizes in order to obtain the best minimum for each localization. For steps when the conjugate gradient descent and parabolic line search were used, the

Polak–Ribiere coefficient [46] sometimes provides better convergence than the default Fletcher–Reeves coefficient [47, 48].

Because we allow the inclusion of unoccupied orbitals, we disentangle the highest-energy conduction bands considered for localization [21]. When including virtual bands, we increase the number of bands from which DLWFs are constructed until the orbitals of interest, usually the ones around the Fermi energy, are converged. Convergence of high-lying virtual bands was found to be difficult; to sidestep this issue, we implement an option allowing the exclusion of specified bands from the cost function convergence criterion. We consider DLWFs converged if  $F$  of the included bands does not change appreciably when higher-energy conduction bands are added. Our code may be found at [42]; more details on the functionality added to **wannier90** are in the Supplemental Material.

## III. RESULTS

We obtain Bloch functions using the PBE density functional [49] in the plane-wave basis, using optimized norm-conserving Vanderbilt pseudopotentials [50] from the PseudoDojo [51]; calculations are performed using the open-source **Quantum ESPRESSO** code suite [52, 53]. For silicon and ethylene, we use a wavefunction kinetic energy cutoff  $E_{\text{cut}} = 60$  Ry; for copper,  $E_{\text{cut}} = 100$  Ry. In all cases,  $E_{\text{cut}}$  for the density is four times that used for the wavefunctions. As mentioned above, DLWFs are computed with a modified version of **wannier90**, with  $\gamma = 0.47714$  unless stated otherwise. We use the SCDM method [54, 55] as the initial guess for dual localization. DLWFs are not always real, so the isoplots seen in Figs. 4–6 are of the densities  $|w_{0i}(\mathbf{r})|^2$ . Lengths are reported in Å and energies in eV.

### A. Silicon

First we consider the well-studied semiconductor silicon in the diamond lattice. We compute the density self-consistently with a  $8 \times 8 \times 8$   $\mathbf{k}$ -mesh, then use a  $4 \times 4 \times 4$   $\mathbf{k}$ -mesh for obtaining virtual Bloch orbitals and DLWFs. We use the experimental lattice parameter  $a = 5.431$  Å [56]. The gap of Si is small, 0.71 eV in our PBE calculation. It is indirect, however; the smallest direct gap in our calculation is 2.56 eV, at  $\mathbf{k} = \Gamma$ . Because of this, even small values of  $\gamma$  separate silicon DLWFs into (approximately) occupied and virtual manifolds.

#### 1. Occupied states

Constructing DLWFs from only the occupied bands of silicon yields Wannier functions which are not degenerate in energy and have different shapes. At  $\gamma = 0.47714$ , the

TABLE I. Energy (near) degeneracies of silicon DLWFs constructed from the occupied, frontier, and converged (30) bands with  $\gamma = 0.47714$ . We call two DLWFs degenerate if their average energies  $\langle w_{\mathbf{0}i} | \tilde{h} | w_{\mathbf{0}i} \rangle$  are within 0.2 eV of one another. The first column is the number of degenerate DLWFs in each set; the other columns give  $\langle w_{\mathbf{0}i} | \tilde{h} | w_{\mathbf{0}i} \rangle$  averaged over the degenerate set. Complete data may be found in the Supplemental Material.

Count	Occupied	Frontier	Converged
1	-3.2290	-3.2341	-3.2341
1	0.5339	0.5282	0.5285
2	3.7185	3.7333	3.7388
4		11.4122	10.6307
2			15.6969

DLWF with lowest average energy  $\langle w_{\mathbf{0}i} | \tilde{h} | w_{\mathbf{0}i} \rangle$  is tetrahedral. The two with highest average energy are degenerate, each having three lobes centered along a Si-Si bond. The shapes and degeneracy patterns are qualitatively equivalent to the four lowest-energy DLWFs in Fig. 2, labeled 1–4 in Fig. 4.

This is in contrast with MLWFs constructed from the same set of bands, all four of which are degenerate, bond-centered tight-binding orbitals [11]. They share the fourfold symmetry of the silicon site. This is a tradeoff between maximally and dually localized Wannier functions: while DLWFs retain information about the underlying energy spectrum, they do not respect the spatial symmetries of the lattice as robustly as MLWFs do. MLWFs may therefore be preferred in calculations of properties like the dipole moment, in which spatial symmetry plays a major role; DLWFs are more naturally suited to energy-dependent methods such as corrections to delocalization error (see IV below).

## 2. Frontier states

We expect the valence bands of semiconductors to yield degenerate MLWFs that approximate bonding molecular orbitals; localizing the same number of low-lying conduction bands with the MLWF procedure often yields degenerate functions of antibonding character. Since the conduction states are entangled with higher-energy bands, Souza *et al.* [21] disentangled 12 bands down to 8 when investigating silicon. Here, we use the same disentanglement with a frozen disentanglement window at the Fermi energy, 6.23 eV. As long as  $\gamma$  is greater than about 0.05, the DLWFs self-organize into (approximately) occupied and virtual manifolds. That is, there are four DLWFs with occupations  $\lambda_{ii} = \langle w_{\mathbf{0}i} | \rho | w_{\mathbf{0}i} \rangle \approx 1$ , and four with  $\lambda_{ii} \approx 0$ . (Here  $\rho$  is the density matrix.) The virtual DLWFs, which have a higher average energy  $\langle w_{\mathbf{0}i} | \tilde{h} | w_{\mathbf{0}i} \rangle$  than the occupied ones, are roughly degenerate for  $0.05 \leq \gamma \leq 0.53$ , as can be seen in Fig. 2. They resemble  $\sigma^*$  antibonding orbitals centered along different Si-Si bonds (see DLWFs

5–8 in Fig. 4), similar to the MLWFs constructed only from low-energy conduction bands [21] or mapped to the conduction band by automated mixing [31]. Like those in the previous section, the occupied DLWFs do not have tight-binding character (as the MLWFs in [21, 31] do), except for the narrow range around  $0.05 \leq \gamma \leq 0.10$ . With a larger penalty for energy variance, a tetrahedral DLWF with lowest average energy appears (labeled 1 in Fig. 4). Between  $\gamma = 0.40$  and  $\gamma = 0.45$ , the threefold degenerate ‘upper valence’ DLWF submanifold splits again. It yields two highest occupied DLWFs centered along bonds, which have the shape of Fig. 4, DLWFs 3–4; and one reminiscent of the  $sp^3$  hybrid in [21], shaped like DLWF 2 in Fig. 4. Note that such degeneracy breaking between sets of DLWFs is associated with sharp changes in both the spatial and energy variance (Fig. 2). As expected, the DLWFs’ spatial variance increases monotonically with  $\gamma$ , while the energy variance decreases.

The band structure interpolated from the DLWFs does not always reproduce the DFA band structure quantitatively when the Brillouin zone is not sampled finely enough or for high-energy conduction bands affected by disentanglement. It is possible that a somewhat finer mesh of  $\mathbf{k}$ -points is required for DLWFs than for MLWFs, because dually localized Wannier functions are not guaranteed to be exponentially localized (compare Section VI.A of [57]). See Supplemental Fig. 5 and the surrounding discussion for the effect of a larger  $\mathbf{k}$ -grid on band structure interpolation in silicon.

In order to show how the mixing parameter  $\gamma$  affects band interpolation along a  $\mathbf{k}$ -path, we calculate the difference between the interpolated eigenvalues  $\tilde{\epsilon}_{\mathbf{k}i}$  and those ( $\epsilon_{\mathbf{k}n}$ ) obtained before disentanglement; the results are shown in Fig. 3. (Note that the low-energy disentangled bands  $i$  of gapped systems can be reliably identified one-to-one with original bands  $n_i$ .) We calculate the mean squared error per band as

$$\bar{\Delta} = \frac{1}{N_w} \sum_i \left[ \frac{1}{N_k} \sum_{\mathbf{k}}^{\text{path}} (\epsilon_{\mathbf{k}n_i} - \tilde{\epsilon}_{\mathbf{k}i})^2 \right]; \quad (23)$$

here, the sum over  $\mathbf{k}$  follows the band structure path, not the Monkhorst-Pack mesh. The interpolation error in Fig. 3 at  $\gamma = 0$  arises primarily from the virtual orbitals; that is, from disentanglement rather than interpolation. The noticeable upticks in interpolation error for the valence states around  $\gamma = 0.4$  and for the conduction states around  $\gamma = 0.5$  are due to groups of degenerate Wannier functions splitting into separate states (Fig. 2). This splitting of degeneracy is due to the energy cost term becoming larger than the spatial cost term for a given DLWF configuration. For a given set of DLWFs, then, lower-degeneracy DLWFs always have a larger spatial spread than their higher-degeneracy counterparts. The larger spatial spread of these lower-degeneracy DLWFs yields a poorer interpolation of the band structure because Wannier function interpolation accuracy relies on rapid spatial decay of the Wannier functions. A comparison of

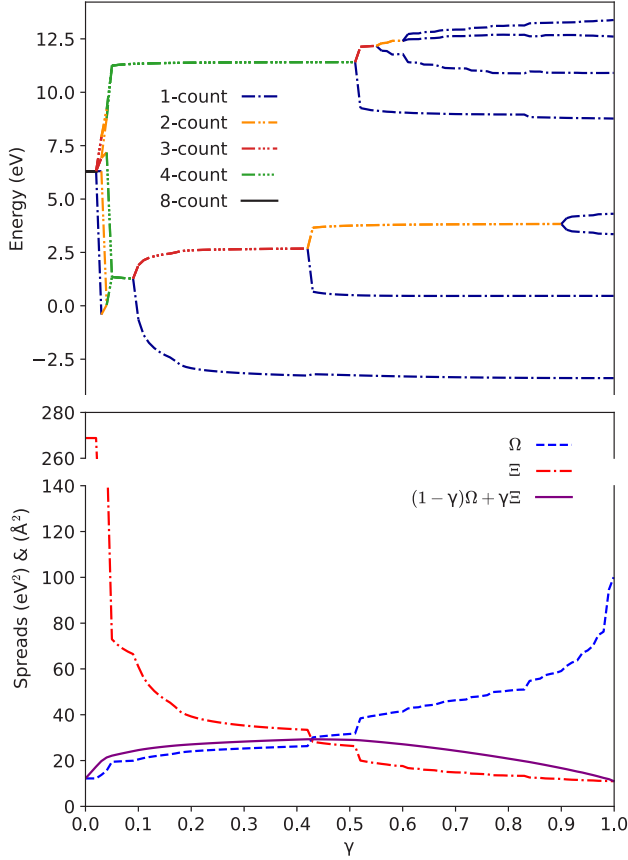


FIG. 2. Top panel: Degeneracy of the DLWFs in silicon as the space-energy mixing  $\gamma$  is varied. As in Table I, we call two DLWFs degenerate if their average energies  $\langle w_{0i} | \tilde{h} | w_{0i} \rangle$  are within 0.2 eV of one another. At  $\gamma = 0$ , all eight (maximally localized) Wannier functions are degenerate  $sp^3$ -like orbitals with occupation  $\lambda_{ii} = 0.5$  and  $\langle w_{0i} | \tilde{h} | w_{0i} \rangle = 6.3$  eV. At  $\gamma = 0.05$ , the DLWFs split into occupied (valence) and virtual (conduction) manifolds. The degeneracy of the occupied DLWFs changes starting at  $\gamma = 0.10$ , while fourfold degeneracy of the virtual DLWFs is not broken until  $\gamma = 0.53$ . Bottom panel: The spatial ( $\Omega$ , blue dashed line), energy ( $\Xi$ , red dot-dashed line), and total (purple solid line) DLWF cost functions for the same silicon system as  $\gamma$  varies. The sharp changes in  $\Omega$  and  $\Xi$  correspond to the splitting of degenerate WFs into qualitatively distinct ones in the top panel. Note the discontinuity in the vertical axis.

interpolated band structure plots at some specific values of  $\gamma$  is provided in the Supplemental Material.

### 3. Converged frontier states

The spatial variances of the highest-energy occupied DLWFs are well converged when 34 bands are disentangled to 30, although the average energy  $\langle w_{0i} | \tilde{h} | w_{0i} \rangle$  of the low-lying, essentially unoccupied DLWFs differ between this case and that with 12 bands disentangled to 8 DLWFs

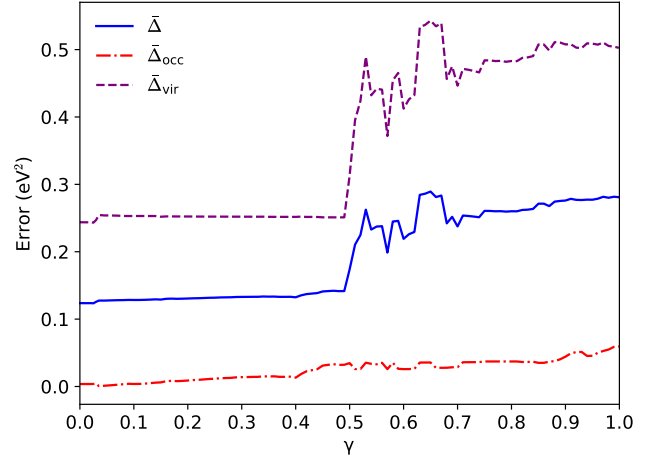


FIG. 3. Band interpolation error from Eq. (23) along the  $\mathbf{k}$ -path used in Fig. 1 (L- $\Gamma$ -X-K-L) for the frontier states of silicon. The solid blue line is the interpolation error averaged over all 8 frontier states; the dash-dotted red line for the 4 highest valence bands; the dashed purple line for the 4 lowest conduction bands.

(Table I). We attribute this to the disentanglement procedure. In III A 2, the virtual DLWFs are drawn almost entirely from the highest-energy Bloch bands, which are most impacted by disentanglement. The lowest-energy DLWFs in this section, on the other hand, are far from the disentanglement window because there are many more Bloch functions, and can therefore be expected to differ somewhat. Fortunately, the value of  $\langle w_{0i} | \tilde{h} | w_{0i} \rangle$  does not impact calculations directly, although (as seen in Fig. 3-4 of the Supplemental Material) the virtual bands are better interpolated from DLWFs constructed from more Bloch orbitals. In addition, those constructed from only 8 disentangled Bloch orbitals are more spatially localized at the same  $\gamma$ ; once again, we attribute this to disentanglement. In the latter case, disentanglement directly smooths the lowest-energy conduction bands  $|\tilde{\psi}_{\mathbf{k}n}\rangle$ , which yields more localized DLWFs [9]. With that said, the DLWFs computed in this section are qualitatively similar to those computed only from occupied or frontier bands, with the same pattern of degeneracies (Table I). We plot isosurfaces of the eight DLWFs of lowest energy in Fig. 4; more data about the individual DLWFs is in the Supplemental Material.

## B. Copper

We next investigate copper in a face-centered cubic lattice, with the experimental lattice parameter  $a = 3.614$  Å [58]. For the self-consistent calculation, we use a  $16 \times 16 \times 16$   $\mathbf{k}$ -mesh; for the virtual states and localization, we use  $10 \times 10 \times 10$   $\mathbf{k}$ -points. Since the unoccupied bands of copper are very steep and energy localization restricts the mixing of bands far apart in energy, we do not re-

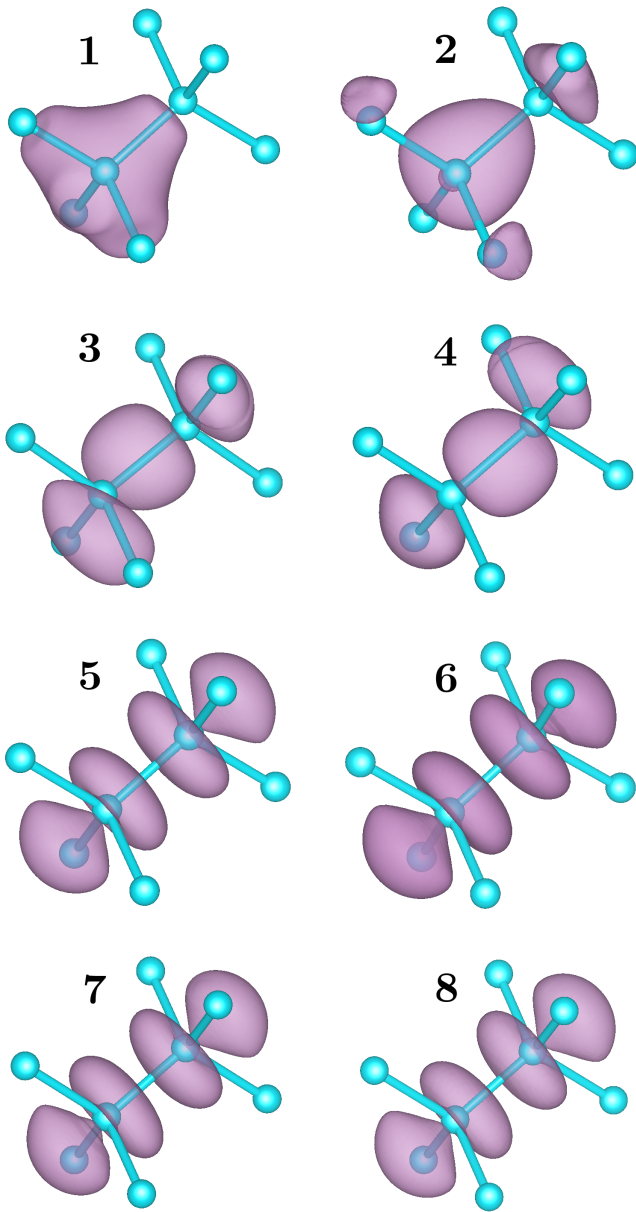


FIG. 4. DLWF ( $\gamma = 0.47714$ ) density isoplots (isovalue 0.6) for silicon labeled in ascending order of  $\langle w_{0i} | \tilde{h} | w_{0i} \rangle$ . These are obtained from 30 disentangled Bloch bands, but the orbitals qualitatively resemble (and have the same pattern of degeneracies as) those obtained from 8 disentangled frontier bands.

quire many bands above the Fermi level. Noting that there are 9.5 electrons per spin channel, we disentangle 23 bands to 17 Wannier functions, with frozen disentanglement required below 40 eV, well above the Fermi energy (17.04 eV). This results in a set of disentangled bands that only differs from the parent DFA at the top of the energy window. When  $\gamma = 0.47714$ , the fully occupied orbitals self-organize into pure *s*, *p*, and *d*-type DLWFs (see Fig. 5). The partially occupied DLWF associated with the frontier band has *d*-type character, but is delocalized

across multiple atoms. Information on individual DLWFs is provided in the Supplemental Material.

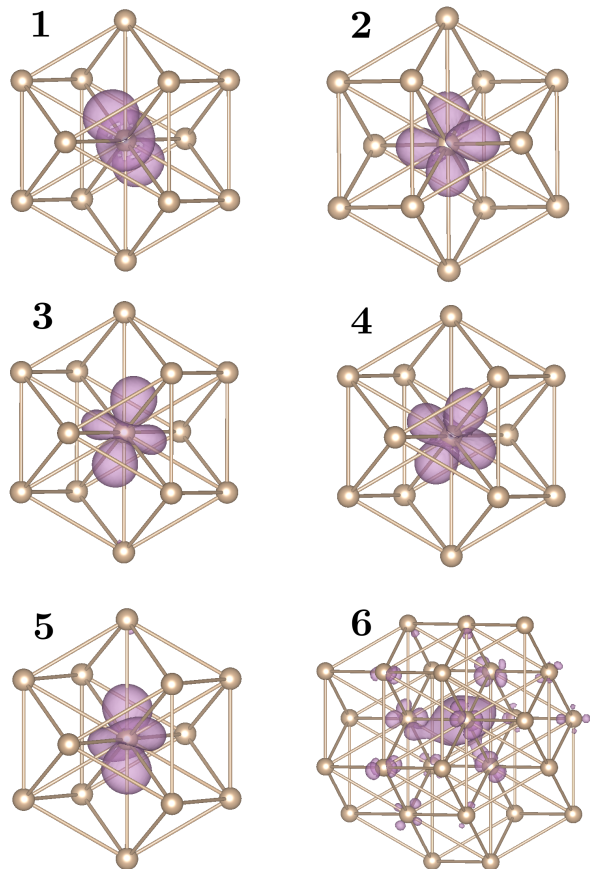


FIG. 5. DLWF ( $\gamma = 0.47714$ ) density isoplots (isovalue 0.6) of copper. These are the six highest-energy occupied DLWFs labeled in ascending order of average energy. DLWF 6 corresponds to the frontier Bloch band and is only partially occupied; it is also more delocalized, so more atoms are shown in its isoplot. (Not shown are four lower-energy DLWFs corresponding to 3*s* and 3*p* orbitals.)

### C. Ethylene

To demonstrate the utility of dual localization in molecules, we simulate ethylene with the geometry from [11]. We use a 10 Å unit cell with the molecule centered at the origin and sample only  $\mathbf{k} = \Gamma$ . Thus, disentanglement is unnecessary, and we construct 36 DLWFs from 36 bands, 6 of which are occupied. Setting  $\gamma = 0.47714$  produces DLWFs closely related to molecular orbitals. The lowest-energy DLWF corresponds to a  $\sigma$  bond between the carbon atoms, and the next four resemble combinations of C–C and C–H bonding orbitals. The highest-energy occupied DLWF corresponds to a  $\pi$  bonding orbital, and the lowest unoccupied DLWF to a  $\pi^*$  antibonding orbital (Fig. 6). The four unoccupied DLWFs next lowest in



energy are degenerate, as noted in the tabulated DLWF information provided in the Supplemental Material, and can be characterized as C–H  $\sigma^*$  orbitals.

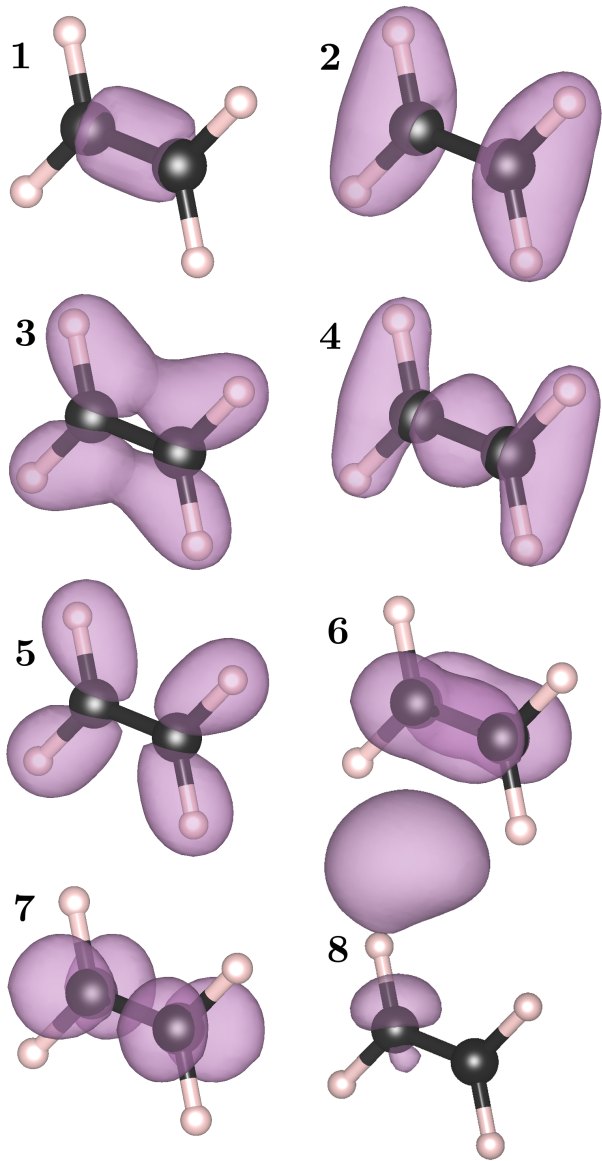


FIG. 6. DLWF density isoplots for ethylene using  $\gamma = 0.47714$ . Isovalues: 160 (DLWF 1), 60 (DLWFs 2–7), 30 (DLWF 8). The isosurface between DLWF 6 and DLWF 8 belongs to DLWF 8.

#### IV. DISCUSSION

DLWFs have frontier orbital character in a variety of systems, from molecules to metals. Those with occupations  $\langle w_{\mathbf{0}i} | \rho | w_{\mathbf{0}i} \rangle \approx 1$  generally appear as bonding or atomic-like orbitals, while the low-lying unoccupied DLWFs ( $\langle w_{\mathbf{0}i} | \rho | w_{\mathbf{0}i} \rangle \approx 0$ ) have antibonding character. In

silicon, they separate naturally into occupied and virtual manifolds. The occupied, atom-centered DLWF (labeled 1 in Fig. 4) is much more localized than the other bond-centered DLWFs, in agreement with the prediction of Kohn [10]. At  $\gamma = 0.47714$ , DLWFs resemble molecular orbitals, such as  $\sigma$  and  $\pi$  bonding orbitals, in ethylene (Fig. 6), and the  $d$  manifold in copper. This shows that DLWFs have the potential to produce chemically relevant frontier orbitals automatically, with no need for manually enforced energy cutoffs or separation of the valence and conduction manifolds.

Because DLWFs offer spatially localized orbitals that describe the frontier orbitals, they can be employed to correct delocalization error in density functional theory. Many methods attempt to correct delocalization error, which describes the failure of density functional approximations to give energy piecewise linear in fractional occupation [3]. They often invoke MLWFs constructed from the valence and low-energy conduction bands separately as localized frontier orbitals [25–27, 29] or use only valence MLWFs [28]. DLWFs have fractional occupations whenever constructed from both valence and conduction bands;  $\langle w_{\mathbf{0}i} | \rho | w_{\mathbf{0}i} \rangle$  is only approximately, not exactly, 1 or 0 in gapped systems. These fractional occupations play an important role in the LOSC method for delocalization error correction [36, 59]. As DLWFs are naturally associated with an energy level, they offer a localized charge description of frontier orbitals for both the occupied and the unoccupied spaces, without requiring an arbitrary limit on the number of conduction bands included.

Analogues to DLWFs have found use in quantum chemistry, describing vibrational states [60] and many-body states for electron transfer [61]. They are called orbitalets, in analogy to wavelets [62], and have proven effective in the molecular LOSC method at improving fundamental gaps of molecules [34, 35, 63], polymer polarizability [64], and chemical reactivity at the frontier energy [37]. We believe that DLWFs will have similar applications in bulk and interfacial systems.

Finally, we comment on the imaginary character sometimes present in DLWFs. Marzari and Vanderbilt [11] conjectured that maximally localized Wannier functions are purely real, up to a global phase. The conjecture was proven by Brouder *et al.* [12] for Wannier functions constructed by minimizing any functional symmetric under time reversal, provided that the optimum is unique. Our cost function  $F$  obeys time-reversal symmetry, and numerical tests show that DLWFs with  $\langle w_{\mathbf{0}i} | \rho | w_{\mathbf{0}i} \rangle \approx 1$  are real. However, we observe substantial imaginary character in DLWFs that have an occupation numerically distinguishable from 1. Even though the arguments in [12] do not differentiate between the occupied and unoccupied manifolds, we conjecture that they do not apply to Wannier functions whose occupation is far from 1. It is possible, however, that the imaginary character of fractionally occupied DLWFs is because  $F$  lacks a unique global minimum.

## V. CONCLUSION

We have shown that including both spatial and energy variance in the localization cost function yields Wannier functions localized both in space and in energy. This allows for Bloch bands widely separated in energy to be included in their construction without mixing arbitrarily, so that DLWFs are in principle a complete basis of localized, orthonormal, translationally symmetric orbitals. Furthermore, the dual localization procedure naturally organizes itself along the Hamiltonian's spectrum, yielding DLWFs with frontier-orbital character.

The ambiguity in the choice of  $\gamma$ , as well as the difficulty in minimizing  $F$  for high-energy conduction bands, suggests seeking an alternative—perhaps approximate—form of DLWFs that do not require optimizing an objec-

tive function. Damle and Lin [65] have proposed such a method, which extends the SCDM method to entangled bands, that approximates MLWFs. It relies on the exponential decay of the off-diagonal elements of  $\rho(\mathbf{r}, \mathbf{r}')$  in space, however, so it is unclear whether it can be adapted to the DLWF cost function.

## ACKNOWLEDGMENTS

We gratefully acknowledge helpful comments from our anonymous referees, and financial support from the National Science Foundation (Grant No. CHE-2154831). A.M. was additionally supported by the Molecular Sciences Software Institute Phase-II Software Fellowship, and J.Z.W. by the National Institutes of Health (Grant No. 5R01GM061870).

- 
- [1] T. Koopmans, Über die Zuordnung von Wellenfunktionen und Eigenwerten zu den Einzelnen Elektronen Eines Atoms, *Physica* **1**, 104 (1934).
  - [2] J. F. Janak, Proof that  $\frac{\partial E}{\partial N_i} = \epsilon_i$  in density-functional theory, *Phys. Rev. B* **18**, 7165 (1978).
  - [3] J. P. Perdew, R. G. Parr, M. Levy, and J. L. Balduz, Density-Functional Theory for Fractional Particle Number: Derivative Discontinuities of the Energy, *Phys. Rev. Lett.* **49**, 1691 (1982).
  - [4] A. J. Cohen, P. Mori-Sánchez, and W. Yang, Fractional charge perspective on the band gap in density-functional theory, *Phys. Rev. B* **77**, 115123 (2008).
  - [5] N. W. Ashcroft and N. D. Mermin, *Solid-State Physics*, 1st ed. (Harcourt, Orlando, FL, 1976).
  - [6] G. H. Wannier, The Structure of Electronic Excitation Levels in Insulating Crystals, *Phys. Rev.* **52**, 191 (1937).
  - [7] W. Kohn, Analytic Properties of Bloch Waves and Wannier Functions, *Phys. Rev.* **115**, 809 (1959).
  - [8] J. des Cloizeaux, Orthogonal Orbitals and Generalized Wannier Functions, *Phys. Rev.* **129**, 554 (1963).
  - [9] J. des Cloizeaux, Energy Bands and Projection Operators in a Crystal: Analytic and Asymptotic Properties, *Phys. Rev.* **135**, A685 (1964).
  - [10] W. Kohn, Construction of Wannier Functions and Applications to Energy Bands, *Phys. Rev. B* **7**, 4388 (1973).
  - [11] N. Marzari and D. Vanderbilt, Maximally localized generalized Wannier functions for composite energy bands, *Phys. Rev. B* **56**, 12847 (1997).
  - [12] C. Brouder, G. Panati, M. Calandra, C. Mourougane, and N. Marzari, Exponential Localization of Wannier Functions in Insulators, *Phys. Rev. Lett.* **98**, 046402 (2007).
  - [13] G. Panati and A. Pisante, Bloch Bundles, Marzari-Vanderbilt Functional and Maximally Localized Wannier Functions, *Commun. Math. Phys.* **322**, 835 (2013).
  - [14] P. L. Silvestrelli and M. Parrinello, Water Molecule Dipole in the Gas and in the Liquid Phase, *Phys. Rev. Lett.* **82**, 3308 (1999).
  - [15] P. L. Silvestrelli and M. Parrinello, Erratum: Water Molecule Dipole in the Gas and in the Liquid Phase [*Phys. Rev. Lett.* **82**, 3308 (1999)], *Phys. Rev. Lett.* **82**, 5415 (1999).
  - [16] P. L. Silvestrelli and M. Parrinello, Structural, electronic, and bonding properties of liquid water from first principles, *The Journal of Chemical Physics* **111**, 3572 (1999).
  - [17] Y.-S. Lee, M. B. Nardelli, and N. Marzari, Band Structure and Quantum Conductance of Nanostructures from Maximally Localized Wannier Functions: The Case of Functionalized Carbon Nanotubes, *Phys. Rev. Lett.* **95**, 076804 (2005).
  - [18] E. Y. Li and N. Marzari, Improving the Electrical Conductivity of Carbon Nanotube Networks: A First-Principles Study, *ACS Nano* **5**, 9726 (2011).
  - [19] M. Shelley, N. Poilvert, A. A. Mostofi, and N. Marzari, Automated quantum conductance calculations using maximally-localised Wannier functions, *Computer Physics Communications* **182**, 2174 (2011).
  - [20] S. Goedecker, Linear scaling electronic structure methods, *Rev. Mod. Phys.* **71**, 1085 (1999).
  - [21] I. Souza, N. Marzari, and D. Vanderbilt, Maximally localized Wannier functions for entangled energy bands, *Phys. Rev. B* **65**, 035109 (2001).
  - [22] R. Resta, *Berry's Phase and Geometric Quantum Distance. Macroscopic Polarization and Electron Localization*, Troisième Cycle de La Physique En Suisse Romande (EPFL, Lausanne, Lausanne, 2000).
  - [23] P. Mori-Sánchez, A. J. Cohen, and W. Yang, Localization and Delocalization Errors in Density Functional Theory and Implications for Band-Gap Prediction, *Phys. Rev. Lett.* **100**, 146401 (2008).
  - [24] N. L. Nguyen, N. Colonna, A. Ferretti, and N. Marzari, Koopmans-Compliant Spectral Functionals for Extended Systems, *Phys. Rev. X* **8**, 021051 (2018).
  - [25] M. Stengel and N. A. Spaldin, Self-interaction correction with Wannier functions, *Phys. Rev. B* **77**, 155106 (2008).
  - [26] G. Borghi, A. Ferretti, N. L. Nguyen, I. Dabo, and N. Marzari, Koopmans-compliant functionals and their performance against reference molecular data, *Phys. Rev. B* **90**, 075135 (2014).
  - [27] J. Ma and L.-W. Wang, Using Wannier functions to improve solid band gap predictions in density functional theory, *Sci. Rep.* **6**, 24924 (2016).

- [28] D. Wing, G. Ohad, J. B. Haber, M. R. Filip, S. E. Gant, J. B. Neaton, and L. Kronik, Band gaps of crystalline solids from Wannier-localization-based optimal tuning of a screened range-separated hybrid functional, *Proc Natl Acad Sci USA* **118**, e2104556118 (2021).
- [29] N. Colonna, R. De Gennaro, E. Linscott, and N. Marzari, Koopmans Spectral Functionals in Periodic Boundary Conditions, *J. Chem. Theory Comput.* **18**, 5435 (2022).
- [30] J. Qiao, G. Pizzi, and N. Marzari, Projectability disentanglement for accurate and automated electronic-structure Hamiltonians, *npj Comput Mater* **9**, 1 (2023).
- [31] J. Qiao, G. Pizzi, and N. Marzari, Automated mixing of maximally localized Wannier functions into target manifolds, *npj Comput Mater* **9**, 1 (2023).
- [32] F. Gygi, J.-L. Fattebert, and E. Schwegler, Computation of Maximally Localized Wannier Functions using a simultaneous diagonalization algorithm, *Computer Physics Communications* **155**, 1 (2003).
- [33] F. Giustino and A. Pasquarello, Mixed Wannier-Bloch Functions for Electrons and Phonons in Periodic Systems, *Phys. Rev. Lett.* **96**, 216403 (2006).
- [34] C. Li, X. Zheng, N. Q. Su, and W. Yang, Localized orbital scaling correction for systematic elimination of delocalization error in density functional approximations, *Nat. Sci. Rev.* **5**, 203 (2018).
- [35] N. Q. Su, A. Mahler, and W. Yang, Preserving Symmetry and Degeneracy in the Localized Orbital Scaling Correction Approach, *J. Phys. Chem. Lett.* **11**, 1528 (2020).
- [36] A. Mahler, J. Williams, N. Q. Su, and W. Yang, Localized orbital scaling correction for periodic systems, *Phys. Rev. B* **106**, 035147 (2022).
- [37] J. Yu, N. Q. Su, and W. Yang, Describing Chemical Reactivity with Frontier Molecular Orbitals, *JACS Au* **2**, 1383 (2022).
- [38] H. J. Monkhorst and J. D. Pack, Special points for Brillouin-zone integrations, *Phys. Rev. B* **13**, 5188 (1976).
- [39] J. M. Foster and S. F. Boys, Canonical Configurational Interaction Procedure, *Rev. Mod. Phys.* **32**, 300 (1960).
- [40] The numerical value of  $C$  is arbitrary; the units given here are those used in the implementation we describe below.
- [41] See the Supplemental Material at [URL will be inserted by publisher] for further details on energy disentanglement; detailed tables and band structures from the DLWFs studied in this work; a discussion of the units of the space-energy mixing parameter  $\gamma$ ; and the modifications we made to **wannier90**. Includes reference [66].
- [42] A. Mahler, *Mtesseract/wannier90: CostSE*, <https://github.com/mtesseract/wannier90> (2024).
- [43] A. A. Mostofi, J. R. Yates, Y.-S. Lee, I. Souza, D. Vanderbilt, and N. Marzari, Wannier90: A tool for obtaining maximally-localised Wannier functions, *Computer Physics Communications* **178**, 685 (2008).
- [44] A. A. Mostofi, J. R. Yates, G. Pizzi, Y.-S. Lee, I. Souza, D. Vanderbilt, and N. Marzari, An updated version of wannier90: A tool for obtaining maximally-localised Wannier functions, *Computer Physics Communications* **185**, 2309 (2014).
- [45] G. Pizzi, V. Vitale, R. Arita, S. Blügel, F. Freimuth, G. Géranton, M. Gibertini, D. Gresch, C. Johnson, T. Koretsune, J. Ibañez-Azpiroz, H. Lee, J.-M. Lihm, D. Marchand, A. Marrazzo, Y. Mokrousov, J. I. Mustafa, Y. Nohara, Y. Nomura, L. Paulatto, S. Poncé, T. Ponweiser, J. Qiao, F. Thöle, S. S. Tsirkin, M. Wierzbowska, N. Marzari, D. Vanderbilt, I. Souza, A. A. Mostofi, and J. R. Yates, Wannier90 as a community code: New features and applications, *J. Phys.: Condens. Matter* **32**, 165902 (2020).
- [46] E. Polak and G. Ribiere, Note sur la convergence de méthodes de directions conjuguées, *R.I.R.O.* **3**, 35 (1969).
- [47] R. Fletcher and C. M. Reeves, Function minimization by conjugate gradients, *The Computer Journal* **7**, 149 (1964).
- [48] W. H. Press, S. A. Teukolsky, W. T. Vetterling, and B. P. Flannery, *Numerical Recipes in FORTRAN: The Art of Scientific Computing*, 2nd ed., Fortran Numerical Recipes, Vol. 1 (Cambridge University Press, The Pitt Building, Trumpington Street, Cambridge CB2 1RP, 1992).
- [49] J. P. Perdew, K. Burke, and M. Ernzerhof, Generalized Gradient Approximation Made Simple, *Phys. Rev. Lett.* **77**, 3865 (1996).
- [50] D. R. Hamann, Optimized norm-conserving Vanderbilt pseudopotentials, *Phys. Rev. B* **88**, 085117 (2013).
- [51] M. J. van Setten, M. Giantomassi, E. Bousquet, M. J. Verstraete, D. R. Hamann, X. Gonze, and G. M. Rignanese, The PseudoDojo: Training and grading a 85 element optimized norm-conserving pseudopotential table, *Computer Physics Communications* **226**, 39 (2018).
- [52] P. Giannozzi, S. Baroni, N. Bonini, M. Calandra, R. Car, C. Cavazzoni, D. Ceresoli, G. L. Chiarotti, M. Cococcioni, I. Dabo, A. Dal Corso, S. de Gironcoli, S. Fabris, G. Fratesi, R. Gebauer, U. Gerstmann, C. Gougousis, A. Kokalj, M. Lazzeri, L. Martin-Samos, N. Marzari, F. Mauri, R. Mazzarello, S. Paolini, A. Pasquarello, L. Paulatto, C. Sbraccia, S. Scandolo, G. Sclauzero, A. P. Seitsonen, A. Smogunov, P. Umari, and R. M. Wentzcovitch, QUANTUM ESPRESSO: A modular and open-source software project for quantum simulations of materials, *J. Phys.: Condens. Matter* **21**, 395502 (2009).
- [53] P. Giannozzi, O. Andreussi, T. Brumme, O. Bunau, M. Buongiorno Nardelli, M. Calandra, R. Car, C. Cavazzoni, D. Ceresoli, M. Cococcioni, N. Colonna, I. Carnimeo, A. Dal Corso, S. de Gironcoli, P. Delugas, R. A. DiStasio, A. Ferretti, A. Floris, G. Fratesi, G. Fugallo, R. Gebauer, U. Gerstmann, F. Giustino, T. Gorni, J. Jia, M. Kawamura, H.-Y. Ko, A. Kokalj, E. Küçükbenli, M. Lazzeri, M. Marsili, N. Marzari, F. Mauri, N. L. Nguyen, H.-V. Nguyen, A. Otero-de-la-Roza, L. Paulatto, S. Poncé, D. Rocca, R. Sabatini, B. Santra, M. Schlipf, A. P. Seitsonen, A. Smogunov, I. Timrov, T. Thonhauser, P. Umari, N. Vast, X. Wu, and S. Baroni, Advanced capabilities for materials modelling with Quantum ESPRESSO, *J. Phys.: Condens. Matter* **29**, 465901 (2017).
- [54] A. Damle, L. Lin, and L. Ying, Compressed Representation of Kohn–Sham Orbitals via Selected Columns of the Density Matrix, *J. Chem. Theory Comput.* **11**, 1463 (2015).
- [55] A. Damle, L. Lin, and L. Ying, SCDM-k: Localized orbitals for solids via selected columns of the density matrix, *Journal of Computational Physics* **334**, 1 (2017).
- [56] T. Hom, W. Kiszewski, and B. Post, Accurate lattice constants from multiple reflection measurements. II. Lattice constants of germanium silicon, and diamond, *J Appl Cryst* **8**, 457 (1975).
- [57] N. Marzari, A. A. Mostofi, J. R. Yates, I. Souza, and D. Vanderbilt, Maximally localized Wannier functions: Theory and applications, *Rev. Mod. Phys.* **84**, 1419 (2012).

- [58] O. J. Rutt, G. R. Williams, and S. J. Clarke, Reversible lithium insertion and copper extrusion in layered oxysulfides, *Chem. Commun.*, 2869 (2006).
- [59] J. Z. Williams and W. Yang, Correcting Delocalization Error in Materials with Localized Orbitals and Linear-Response Screening (2024), arXiv:2406.07351 [cond-mat, physics:physics].
- [60] R. Dawes and T. Carrington, Jr., Using simultaneous diagonalization and trace minimization to make an efficient and simple multidimensional basis for solving the vibrational Schrödinger equation, *The Journal of Chemical Physics* **124**, 054102 (2006).
- [61] J. E. Subotnik, R. J. Cave, R. P. Steele, and N. Shenvi, The initial and final states of electron and energy transfer processes: Diabatization as motivated by system-solvent interactions, *The Journal of Chemical Physics* **130**, 234102 (2009).
- [62] I. Daubechies, *Ten Lectures on Wavelets*, CBMS-NSF Regional Conference Series in Applied Mathematics No. 61 (Society for Industrial and Applied Mathematics, 1992).
- [63] Y. Mei, Z. Chen, and W. Yang, Self-Consistent Calculation of the Localized Orbital Scaling Correction for Correct Electron Densities and Energy-Level Alignments in Density Functional Theory, *J. Phys. Chem. Lett.* **11**, 10269 (2020).
- [64] Y. Mei, N. Yang, and W. Yang, Describing polymer polarizability with localized orbital scaling correction in density functional theory, *J. Chem. Phys.* **154**, 054302 (2021).
- [65] A. Damle and L. Lin, Disentanglement via Entanglement: A Unified Method for Wannier Localization, *Multiscale Model. Simul.* **16**, 1392 (2018).
- [66] E. Tiesinga, P. J. Mohr, D. B. Newell, and B. N. Taylor, The 2018 CODATA Recommended Values of the Fundamental Physical Constants, <https://physics.nist.gov/cuu/Constants/index.html> (2020).



# Supplemental Material for Wannier Functions Dually Localized in Space and Energy

Aaron Mahler

*Duke University, Department of Physics, Durham, NC 27708*

Jacob Z. Williams

*Duke University, Department of Chemistry, Durham, NC 27708*

Neil Qiang Su

*Department of Chemistry, Key Laboratory of Advanced Energy Materials Chemistry  
(Ministry of Education) and Renewable Energy Conversion and Storage Center (RECAST),*

*Nankai University, Tianjin 300071, China and*

*Duke University, Department of Chemistry, Durham, NC 27708*

Weitao Yang\*

*Duke University, Department of Chemistry, Durham, NC 27708 and*

*Duke University, Department of Physics, Durham, NC 27708*

(Dated: May 20, 2025)

## I. ORBITAL OCCUPATIONS

Because we include unoccupied Bloch orbitals, we must consider orbital occupations when considering the projector onto the occupied manifold (that is, the one-particle density matrix):

$$P_{\text{occ}} = \frac{1}{N_k} \sum_{\mathbf{k}n} f_{\mathbf{k}n} |\psi_{\mathbf{k}n}\rangle \langle \psi_{\mathbf{k}n}|, \quad (1)$$

where  $f_{\mathbf{k}n} = \langle \psi_{\mathbf{k}n} | P_{\text{occ}} | \psi_{\mathbf{k}n} \rangle$  is the occupation of  $|\psi_{\mathbf{k}n}\rangle$  ( $f_{\mathbf{k}n} = 0$  or  $1$  if the system is an insulator). If the DLWFs are constructed solely from the occupied bands ( $f_{\mathbf{k}n} = 1$ ), then also  $P_{\text{occ}} = \sum_{\mathbf{k}n} |w_{\mathbf{R}n}\rangle \langle w_{\mathbf{R}n}|$ . However, allowing valence and conduction bands to mix means that  $P_{\text{occ}}$  is no longer diagonal in the Wannier basis:

$$P_{\text{occ}} = \sum_{\mathbf{R}\mathbf{T}mn} \lambda_{\mathbf{R}\mathbf{T}mn} |w_{\mathbf{R}m}\rangle \langle w_{\mathbf{T}n}|, \quad (2)$$

where  $\lambda_{\mathbf{R}\mathbf{T}mn} = \langle w_{\mathbf{R}m} | P_{\text{occ}} | w_{\mathbf{T}n} \rangle$  is the pairwise occupation between two Wannier functions. The matrix  $(\lambda_{\mathbf{R}\mathbf{T}mn})$  is Hermitian, and while the effective occupation  $\lambda_{\mathbf{R}\mathbf{R}nn}$  of  $|w_{\mathbf{R}n}\rangle$  is not in general an integer, it does satisfy  $0 \leq \lambda_{\mathbf{R}\mathbf{R}nn} \leq 1$ .

We can also write  $P_{\text{occ}}$  in the basis of transformed Bloch orbitals as

$$\begin{aligned} P_{\text{occ}} &= \frac{1}{N_k^2} \sum_{\mathbf{k}m} \sum_{\mathbf{q}n} \langle \phi_{\mathbf{k}m} | P_{\text{occ}} | \phi_{\mathbf{q}n} \rangle |\phi_{\mathbf{k}m}\rangle \langle \phi_{\mathbf{q}n}| \\ &= \frac{1}{N_k} \sum_{\mathbf{k}mn} \lambda_{\mathbf{k}mn} |\phi_{\mathbf{k}m}\rangle \langle \phi_{\mathbf{q}n}|, \end{aligned} \quad (3)$$

where  $|\phi_{\mathbf{k}n}\rangle = \sum_m U_{mn}^{\mathbf{k}} |\psi_{\mathbf{k}m}\rangle$ . The pairwise occupation  $\lambda_{\mathbf{k}mn}$  between  $|\phi_{\mathbf{k}m}\rangle$  and  $|\phi_{\mathbf{k}n}\rangle$  is not diagonal in the band index  $n$  if valence and conduction bands are mixed by  $U^{\mathbf{k}}$ , although it does remain diagonal in  $\mathbf{k}$ ; as in the Wannier basis,  $0 \leq \lambda_{\mathbf{k}nn} \leq 1$ .

The local occupation matrices  $(\lambda_{\mathbf{k}mn})$  and  $(\lambda_{\mathbf{R}\mathbf{T}mn})$  are related by discrete Fourier transforms; and their traces, restricted to a single  $\mathbf{k}$  point (or unit cell  $\mathbf{R}$ ), give the number of electrons below the Fermi energy at  $\mathbf{k}$  (in the unit cell  $\mathbf{R}$ ). That is,

$$\text{Tr}_{\mathbf{k}} (\lambda_{\mathbf{k}mn}) = \sum_n \lambda_{\mathbf{k}nn} = N_{\text{occ}}(\mathbf{k}), \quad (4)$$

and

$$\text{Tr}_{\mathbf{R}} (\lambda_{\mathbf{R}\mathbf{T}mn}) = \sum_n \lambda_{\mathbf{R}\mathbf{R}nn} = \frac{1}{N_k} \sum_{\mathbf{k}} N_{\text{occ}}(\mathbf{k}). \quad (5)$$

---

\* weitao.yang@duke.edu

## II. GAUGE-INVARIANT ENERGY COST WITH DISENTANGLEMENT

The projector  $\tilde{P}$  onto the subspace spanned by the disentangled bands  $|\tilde{\psi}_{\mathbf{k}i}\rangle$  can be written in either the disentangled Bloch or Wannier basis:

$$\tilde{P} = \sum_{\mathbf{k}i} |\tilde{\psi}_{\mathbf{k}i}\rangle \langle \tilde{\psi}_{\mathbf{k}i}| = \sum_{\mathbf{R}i} |w_{\mathbf{R}i}\rangle \langle w_{\mathbf{R}i}|. \quad (6)$$

Then we can write the gauge-invariant part of the energy cost  $\Xi$  as

$$\begin{aligned} \Xi_I &= \sum_i \left[ \langle w_{\mathbf{0}i} | \tilde{h}^2 | w_{\mathbf{0}i} \rangle - \sum_{\mathbf{R}j} |\langle w_{\mathbf{R}j} | \tilde{h} | w_{\mathbf{0}i} \rangle|^2 \right] \\ &= \sum_i \left[ \langle w_{\mathbf{0}i} | \tilde{h}^2 | w_{\mathbf{0}i} \rangle - \sum_{\mathbf{R}j} \langle w_{\mathbf{0}i} | \tilde{h} | w_{\mathbf{R}j} \rangle \langle w_{\mathbf{R}j} | \tilde{h} | w_{\mathbf{0}i} \rangle \right] \\ &= \sum_i \left[ \langle w_{\mathbf{0}i} | \tilde{h}^2 | w_{\mathbf{0}i} \rangle - \langle w_{\mathbf{0}i} | \tilde{h} \left( \sum_{\mathbf{R}j} |w_{\mathbf{R}j}\rangle \langle w_{\mathbf{R}j}| \right) \tilde{h} | w_{\mathbf{0}i} \rangle \right] \\ &= \sum_i \left[ \langle w_{\mathbf{0}i} | \tilde{h}^2 | w_{\mathbf{0}i} \rangle - \langle w_{\mathbf{0}i} | \tilde{h} \tilde{P} \tilde{h} | w_{\mathbf{0}i} \rangle \right] = \sum_i \langle w_{\mathbf{0}i} | \tilde{h} I \tilde{h} - \tilde{h} \tilde{P} \tilde{h} | w_{\mathbf{0}i} \rangle \\ &= \sum_i \langle w_{\mathbf{0}i} | \tilde{h}^2 | w_{\mathbf{0}i} \rangle - \sum_i \langle w_{\mathbf{0}i} | \tilde{h} \tilde{P} \tilde{h} | w_{\mathbf{0}i} \rangle = \\ &= \text{Tr}_c [\tilde{P} \tilde{h}^2] - \text{Tr}_c [\tilde{P} \tilde{h} \tilde{P} \tilde{h}]. \end{aligned} \quad (7)$$

Noting that

$$\begin{aligned} \tilde{P} \tilde{h} &= \left( \sum_{\mathbf{k}i} |\tilde{\psi}_{\mathbf{k}i}\rangle \langle \tilde{\psi}_{\mathbf{k}i}| \right) \left( \sum_{\mathbf{k}'i'} \tilde{\varepsilon}_{\mathbf{k}'i'} |\tilde{\psi}_{\mathbf{k}'i'}\rangle \langle \tilde{\psi}_{\mathbf{k}'i'}| \right) \\ &= \sum_{\mathbf{k}\mathbf{k}'ii'} \tilde{\varepsilon}_{\mathbf{k}'i'} |\tilde{\psi}_{\mathbf{k}i}\rangle \langle \tilde{\psi}_{\mathbf{k}i}| \tilde{\psi}_{\mathbf{k}'i'} \rangle \langle \tilde{\psi}_{\mathbf{k}'i'}| \\ &= \sum_{\mathbf{k}i} \tilde{\varepsilon}_{\mathbf{k}i} |\tilde{\psi}_{\mathbf{k}i}\rangle \langle \tilde{\psi}_{\mathbf{k}i}| \\ &= \tilde{h}, \end{aligned} \quad (8)$$

whence  $\tilde{P} \tilde{h}^2 = \tilde{P} \tilde{h} \tilde{P} \tilde{h} = \tilde{h}^2$ , we obtain that

$$\Xi_I = \text{Tr}_c [\tilde{P} \tilde{h}^2] - \text{Tr}_c [\tilde{P} \tilde{h} \tilde{P} \tilde{h}] = 0. \quad (9)$$

## III. APPENDIX OF TABLES

This section shows the spatial center  $(\langle r_x \rangle, \langle r_y \rangle, \langle r_z \rangle)$ , spatial variance  $\langle \Delta r^2 \rangle$ , average energy  $\langle h \rangle$ , energy variance  $\langle \Delta h^2 \rangle$ , and occupation  $\lambda_{\mathbf{0}ii} = \langle w_{\mathbf{0}i} | \rho | w_{\mathbf{0}i} \rangle$  of the individual

DLWFs presented in the Results section of the main text. The index is ordered from lowest to highest energy, starting at 1. Thus, the index in Table III (Table IV, Table V) below corresponds to the DLWF density isoplot labels in Fig. 4 (Fig. 5, Fig. 6) of the main text.

### A. Silicon

TABLE I: Spatial and energy information per DLWF when only using the valence states of silicon.

index	$\langle r_x \rangle$	$\langle r_y \rangle$	$\langle r_z \rangle$	$\langle \Delta r^2 \rangle$	$\langle h \rangle$	$\langle \Delta h^2 \rangle$	$\lambda_{0ii}$
1	0.6280	0.7208	0.7298	2.346988	-3.228980	1.700047	1.000000
2	-1.1404	-0.8386	-0.2173	4.867715	0.533916	3.614710	1.000000
3	0.9968	0.0737	1.6037	4.481121	3.718522	1.627641	1.000000
4	-0.2461	0.0736	0.3609	4.481166	3.718535	1.627611	1.000000

TABLE II: Spatial and energy information per DLWF when using 12 bands disentangled to produce 8 DLWFs.

index	$\langle r_x \rangle$	$\langle r_y \rangle$	$\langle r_z \rangle$	$\langle \Delta r^2 \rangle$	$\langle h \rangle$	$\langle \Delta h^2 \rangle$	$\lambda_{0ii}$
1	0.6393	0.7274	0.7274	2.358287	-3.234109	1.681093	0.999994
2	-0.5300	-0.2339	-0.2340	4.840094	0.528172	3.587587	0.999599
3	-1.4288	-1.1217	0.3475	4.369317	3.733272	1.664589	0.998669
4	1.2869	0.3475	1.5940	4.369209	3.733309	1.664698	0.998666
5	0.0548	0.0466	0.0468	3.821754	11.392893	4.591103	0.000972
6	-0.0529	1.4009	1.4007	3.817564	11.396780	4.589852	0.000944
7	-1.3560	-0.0132	4.0654	3.822250	11.428582	4.551941	0.000580
8	-1.3552	1.3505	2.7017	3.819881	11.430745	4.553351	0.000577

TABLE III: Spatial and energy information per DLWF for silicon using 34 bands disentangled to 30 bands.

index	$\langle r_x \rangle$	$\langle r_y \rangle$	$\langle r_z \rangle$	$\langle \Delta r^2 \rangle$	$\langle h \rangle$	$\langle \Delta h^2 \rangle$	$\lambda_{0ii}$
-------	-----------------------	-----------------------	-----------------------	------------------------------	---------------------	------------------------------	-----------------



1	-0.7273	-0.6394	-0.7274	2.357579	-3.234141	1.681126	0.999992
2	0.2355	0.5311	0.2360	4.824702	0.528461	3.594108	0.999453
3	-0.3476	-1.2893	-1.5917	4.296241	3.738779	1.693098	0.997848
4	-1.5941	-1.2878	-0.3466	4.294985	3.738866	1.692406	0.997860
5	-0.0505	2.6608	2.7073	4.845865	10.548782	4.084945	0.001534
6	1.2678	0.0730	1.2995	4.853594	10.569209	4.085532	0.001481
7	1.4140	-1.3094	-2.7687	4.916316	10.693759	4.064643	0.000875
8	0.0238	1.3053	1.3575	4.907699	10.711160	4.088860	0.000869
9	-0.0182	0.0123	0.0392	8.239568	15.653925	3.218761	0.000047
10	-0.8270	-0.8582	-1.3807	8.298693	15.739891	2.969253	0.000037
11	0.1125	-1.2840	-1.3794	8.389856	18.404274	1.924312	0.000001
12	-0.7443	-0.7126	0.0674	8.252689	18.922132	1.841812	0.000002
13	1.0858	-0.0787	1.4867	8.336248	19.346286	2.670695	0.000001
14	-0.1180	-1.1155	1.2004	9.336795	21.777131	3.725877	0.000000
15	0.0191	-1.2920	-1.3532	8.073594	25.390255	2.437707	0.000000
16	0.0175	0.0323	-0.0157	8.196600	25.395202	2.166016	0.000000
17	1.3469	0.2140	1.1390	8.188723	25.429163	2.396005	0.000000
18	-1.4098	0.0256	-1.3264	7.304936	25.916725	3.080916	0.000000
19	1.3965	0.0338	-1.3458	9.008920	26.269281	2.215705	0.000000
20	0.3826	0.3316	0.4795	10.802935	29.338486	3.072971	0.000000
21	-0.0229	-2.7464	-2.7040	8.376918	31.775110	3.252854	0.000000
22	-1.3644	-2.7038	1.3521	8.258431	31.791921	3.342923	0.000000
23	-0.0453	-1.3281	-1.3151	8.891537	32.291000	2.209553	0.000000
24	-0.0594	-1.3083	1.3658	9.803869	34.805345	3.125115	0.000000
25	1.1648	-1.2274	0.1947	9.635747	35.629707	3.195436	0.000000
26	-2.6160	-0.0473	0.0126	9.687295	35.795476	3.419050	0.000000
27	2.5350	-0.1019	-2.5121	9.086322	37.532297	3.298730	0.000000
28	1.3284	-0.0261	-1.3222	8.512641	39.136116	3.739278	0.000000
29	0.0396	2.7316	-0.0278	9.142814	39.527945	3.099532	0.000000
30	0.0056	1.3209	1.3000	9.366045	40.314612	2.403746	0.000000

## B. Copper

TABLE IV. Spatial and energy information per DLWF for copper.

index	$\langle r_x \rangle$	$\langle r_y \rangle$	$\langle r_z \rangle$	$\langle \Delta r^2 \rangle$	$\langle h \rangle$	$\langle \Delta h^2 \rangle$	$\lambda_{0ii}$
01	-0.0000	0.0000	-0.0000	0.155525	-95.528687	0.000018	1.000000
02	0.0000	0.0000	0.0000	0.186959	-52.928957	0.000814	1.000000
03	0.0000	-0.0000	0.0000	0.186943	-52.928955	0.000811	1.000000
04	-0.0000	-0.0000	-0.0000	0.186958	-52.928954	0.000811	1.000000
05	-0.1631	-0.0051	0.0045	1.326589	13.553628	3.061090	0.996669
06	-0.0038	-0.0046	-0.0073	0.705379	14.072693	1.235276	0.996415
07	-0.0063	0.0014	-0.0177	0.793226	14.078952	1.528006	0.996099
08	-0.0068	-0.0050	0.0046	0.709318	14.085334	1.248489	0.996337
09	0.0096	0.0045	-0.0013	0.803549	14.121215	1.528358	0.996831
10	1.0363	0.9041	-0.8420	4.926801	16.988522	7.848977	0.516482
11	0.6418	-1.0563	-0.3213	7.008280	26.141562	16.535585	0.000001
12	-0.4665	-0.0404	1.4063	7.196124	32.475400	19.176457	0.000000
13	-0.4218	1.0018	1.0964	7.318156	32.739401	20.308781	0.000000
14	0.0123	0.0419	-0.0969	12.324220	39.582046	8.504523	0.000000
15	1.1162	-0.7577	-1.2117	13.706412	45.246294	12.532017	0.001148
16	1.1295	-1.5696	-1.3568	11.206204	51.485678	15.577288	0.000009
17	1.1818	-0.9269	0.0903	8.954952	55.296748	12.405831	0.000009

### C. Ethylene

TABLE V: Spatial and energy information per DLWF for ethylene, truncated to the lowest 20 states.

index	$\langle r_x \rangle$	$\langle r_y \rangle$	$\langle r_z \rangle$	$\langle \Delta r^2 \rangle$	$\langle h \rangle$	$\langle \Delta h^2 \rangle$	$\lambda_{0ii}$
1	-0.0000	-0.0000	0.0000	0.983945	-18.612524	0.000174	1.000000
2	0.0001	0.0000	0.0000	1.784198	-13.889465	0.000596	0.999997
3	0.0002	-0.0000	-0.0001	1.633431	-11.218850	0.003959	0.999974
4	-0.0004	0.0000	0.0000	1.497676	-9.940055	0.005812	0.999947
5	-0.0010	-0.0000	-0.0000	2.015195	-8.185370	0.007015	0.999939
6	0.0000	0.0000	-0.0002	1.329210	-6.559715	0.010217	0.999856
7	0.0007	0.0000	0.0014	2.009921	-0.717311	0.135739	0.000000
8	-1.1695	2.1974	-0.1999	3.337830	1.292702	1.286921	0.000025
9	-1.1696	-2.1974	-0.2001	3.337846	1.292738	1.286973	0.000025
10	2.2760	-1.8212	-0.0673	3.315293	1.349986	1.214562	0.000036
11	2.2761	1.8212	-0.0673	3.315328	1.350045	1.214551	0.000036
12	-3.3293	0.0001	-0.0157	3.786638	1.493888	1.128354	0.000011
13	-0.0724	0.0004	-2.7003	3.546867	1.955814	1.377605	0.000052
14	-0.0642	1.5299	2.4554	4.019978	2.136463	1.134380	0.000044
15	-0.0651	-1.5302	2.4552	4.020222	2.136698	1.134326	0.000044
16	-0.1124	3.2622	-3.9195	4.562633	2.820583	1.205123	0.000002
17	-0.1124	-3.2610	-3.9198	4.562800	2.820617	1.205088	0.000002
18	-4.4466	-3.2543	-0.1016	4.613289	2.977994	1.161815	0.000002
19	-4.4465	3.2544	-0.1015	4.613393	2.978025	1.161790	0.000002
20	-3.4117	4.9992	3.3338	4.192816	2.989893	1.415940	0.000000

#### IV. BAND STRUCTURES

Here we show the disentangled band structures used for the systems reported in the main text. Observe that the disentangled band structure agrees almost exactly with the full band structure near the Fermi energy. We found that DLWFs with a mixing parameter of  $\gamma = 0.01$  gave the best interpolation, which was slightly better than using  $\gamma = 0.0$  (MLWF) and noticeably better than the value of  $\gamma = 0.47714$  used in the isosurface plots. See Supplemental Sec. IV A for details.

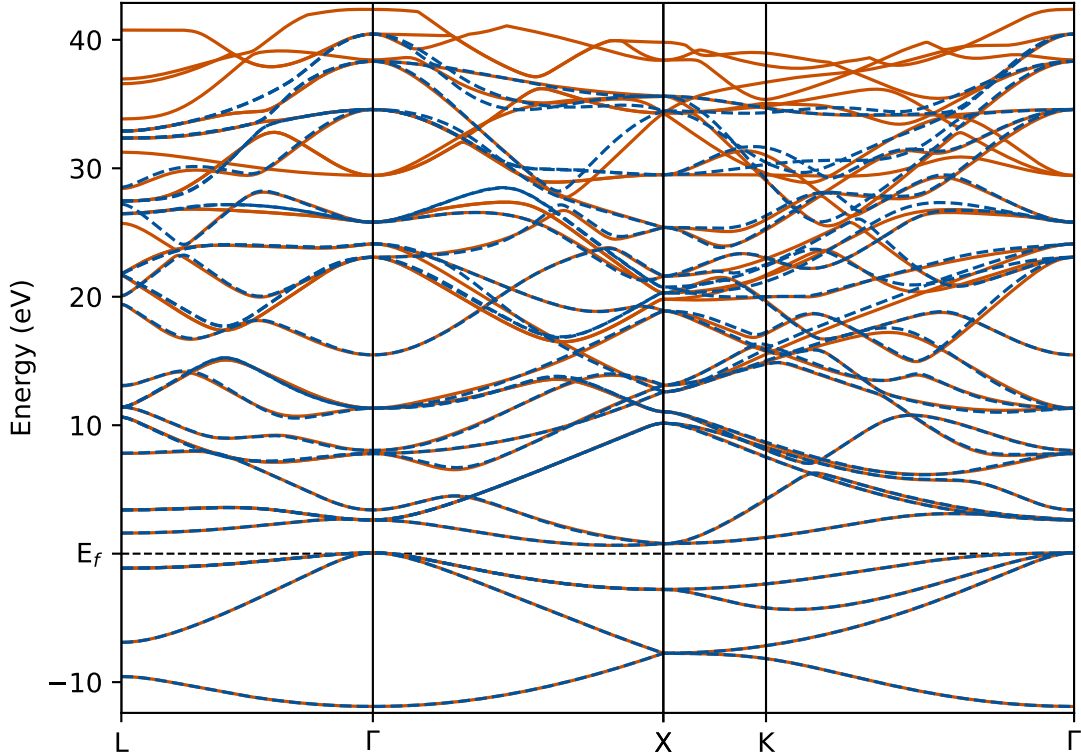


FIG. 1. Disentangled band structure of silicon used for the isosurface plots in the main text. The solid orange lines are 34 bands from a non-self-consistent calculation in `Quantum ESPRESSO` with the zero point of the  $y$ -axis set at the Fermi energy. The dashed blue lines are 30 disentangled bands interpolated along the path through the Brillouin zone using DLWFs with a mixing parameter of  $\gamma = 0.01$ .



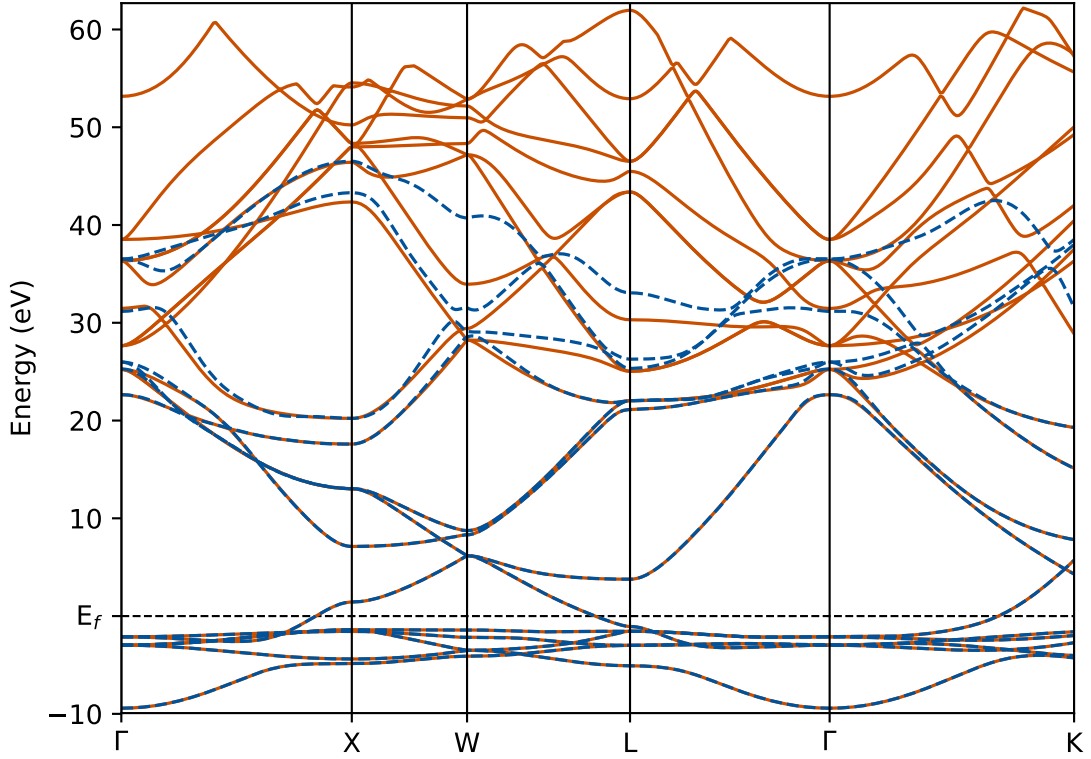


FIG. 2. Disentangled band structure of copper used for the isosurface plots in the main text. The solid orange lines are 23 bands from a non-SCF calculation in `Quantum ESPRESSO`, and the energy axis is zeroed at the Fermi energy. The dashed blue lines are 17 disentangled bands interpolated along the path through the Brillouin zone using DLWFs with a mixing parameter of  $\gamma = 0.01$ .

### A. Interpolated Band Structure Errors in Silicon

Here we show some interpolated band structure plots for specific values of  $\gamma$  in the case of silicon. The plots shown in Figs. 3a–3f are for 12 bands disentangled to produce 8 Wannier functions, the average interpolation error which is reported in the main text. For the case of 34 bands disentangled down to 30, the average squared error for the band interpolation along the path in Figs. 4a–4e is (a) 0.192989, (b) 0.176692, (c) 0.271211, (d) 0.411963, and (e) 0.695313 eV<sup>2</sup>. Since the case of  $\gamma = 0.01$  is slightly better than the MLWF case of  $\gamma = 0.0$  we use this value for the band structure shown in the main text and previous section.

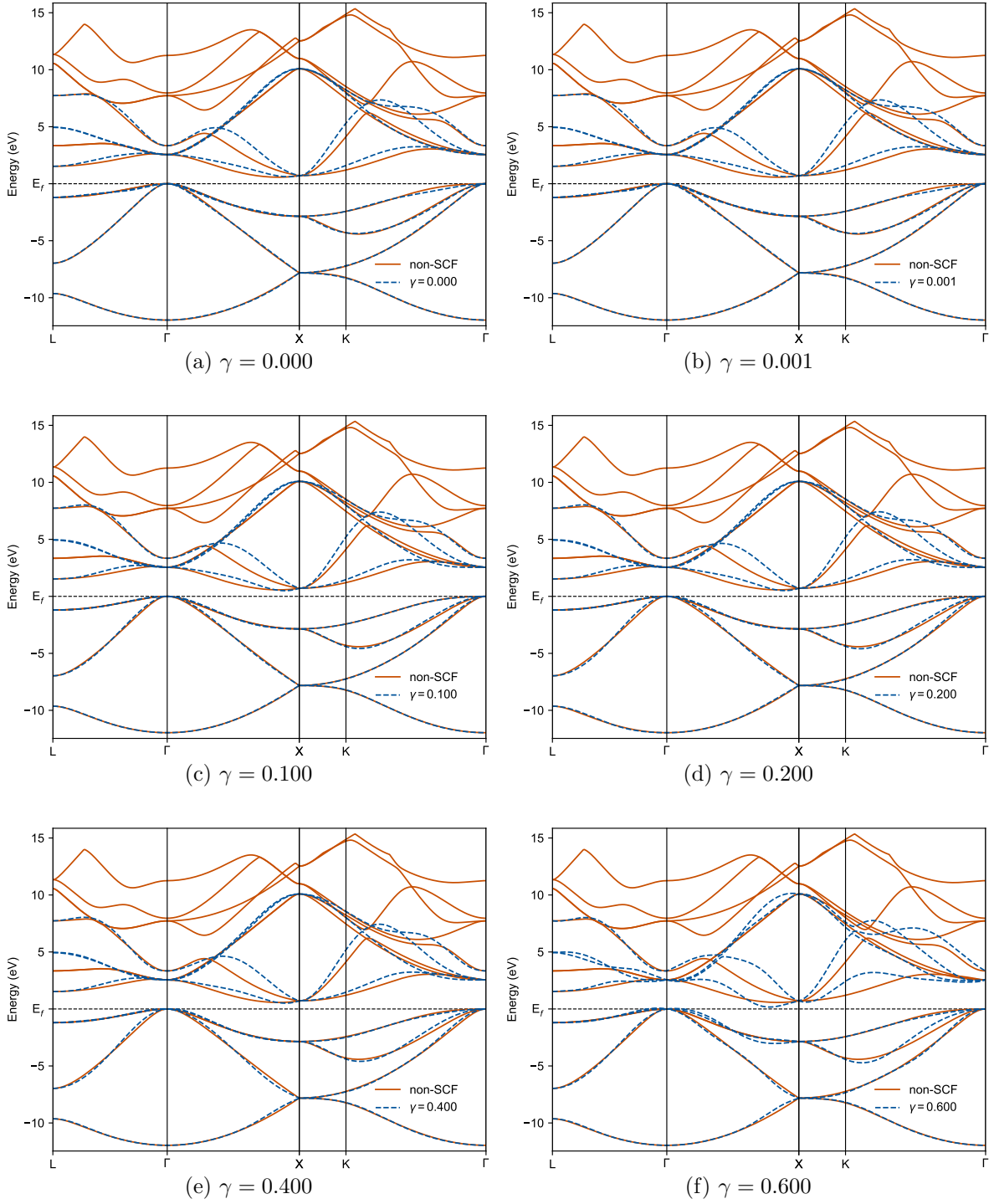


FIG. 3. Interpolated band structures for the frontier states of silicon (12 bands and 8 Wannier functions) for varying values of  $\gamma$ .

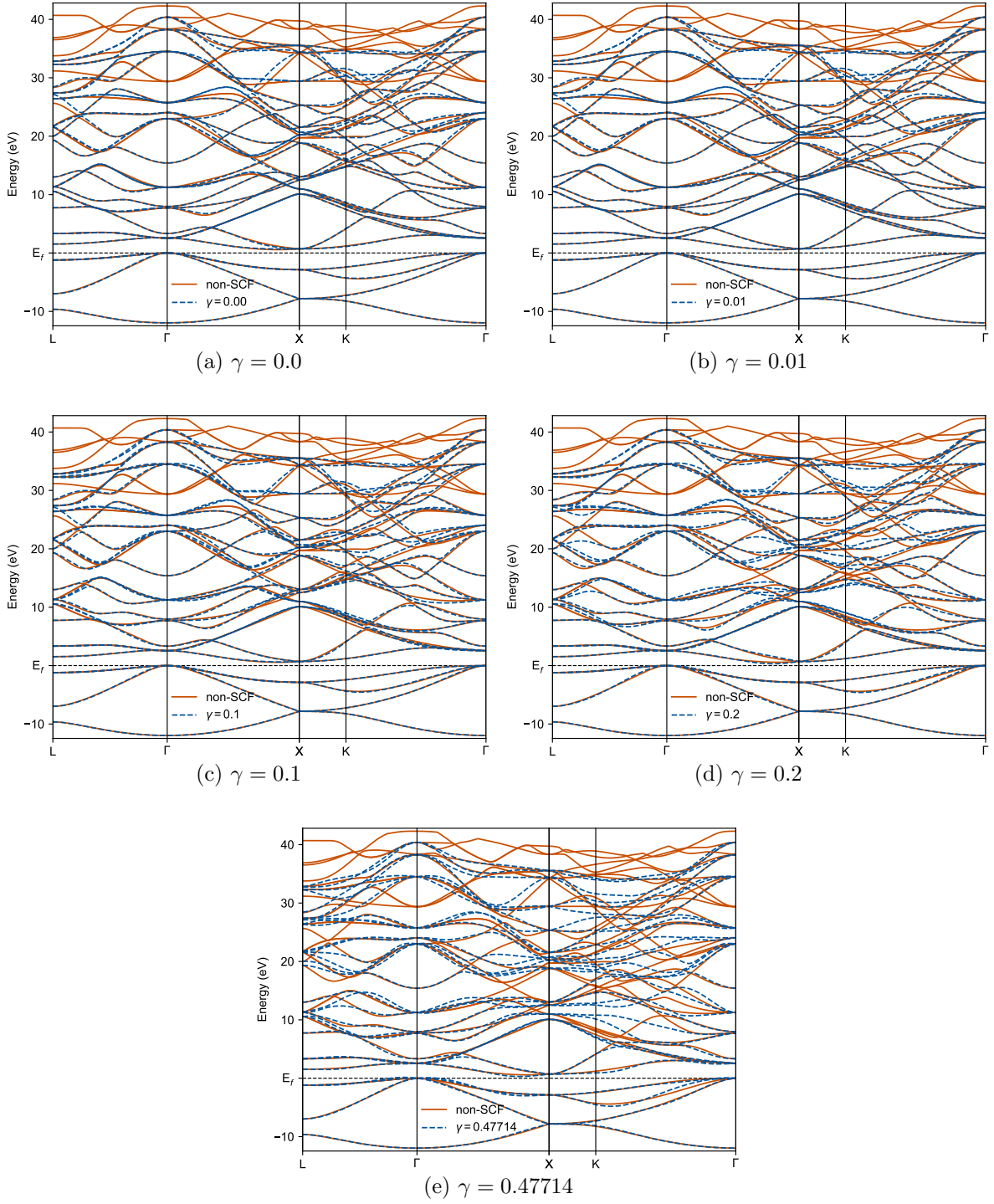


FIG. 4. Interpolated band structures for the converged states of silicon (34 bands and 30 Wannier functions) for varying values of  $\gamma$ .

## B. Band structure interpolation and Brillouin zone sampling

With 12 bands disentangled to 8 DLWFs (the left column of Fig. 5), we do not reconstruct the conduction bands quantitatively because they are affected directly by the disentanglement procedure. The same is true of the highest-energy conduction bands in the right column, but they are far above the Fermi energy. Regardless, the frontier bands are reproduced fairly accurately. Some oscillations in the low-lying DLWF conduction bands, relative to the DFA bands, can be seen even with 28 DLWFs (Fig. 5b); this is ameliorated for larger  $\mathbf{k}$ -samplings. These oscillations do affect the DLWF-interpolated prediction for the conduction band minimum in silicon, which does not lie on a high-symmetry  $\mathbf{k}$ -point. When it is critical to reproduce the (DFA) conduction band minimum accurately, a denser sampling is thus recommended.

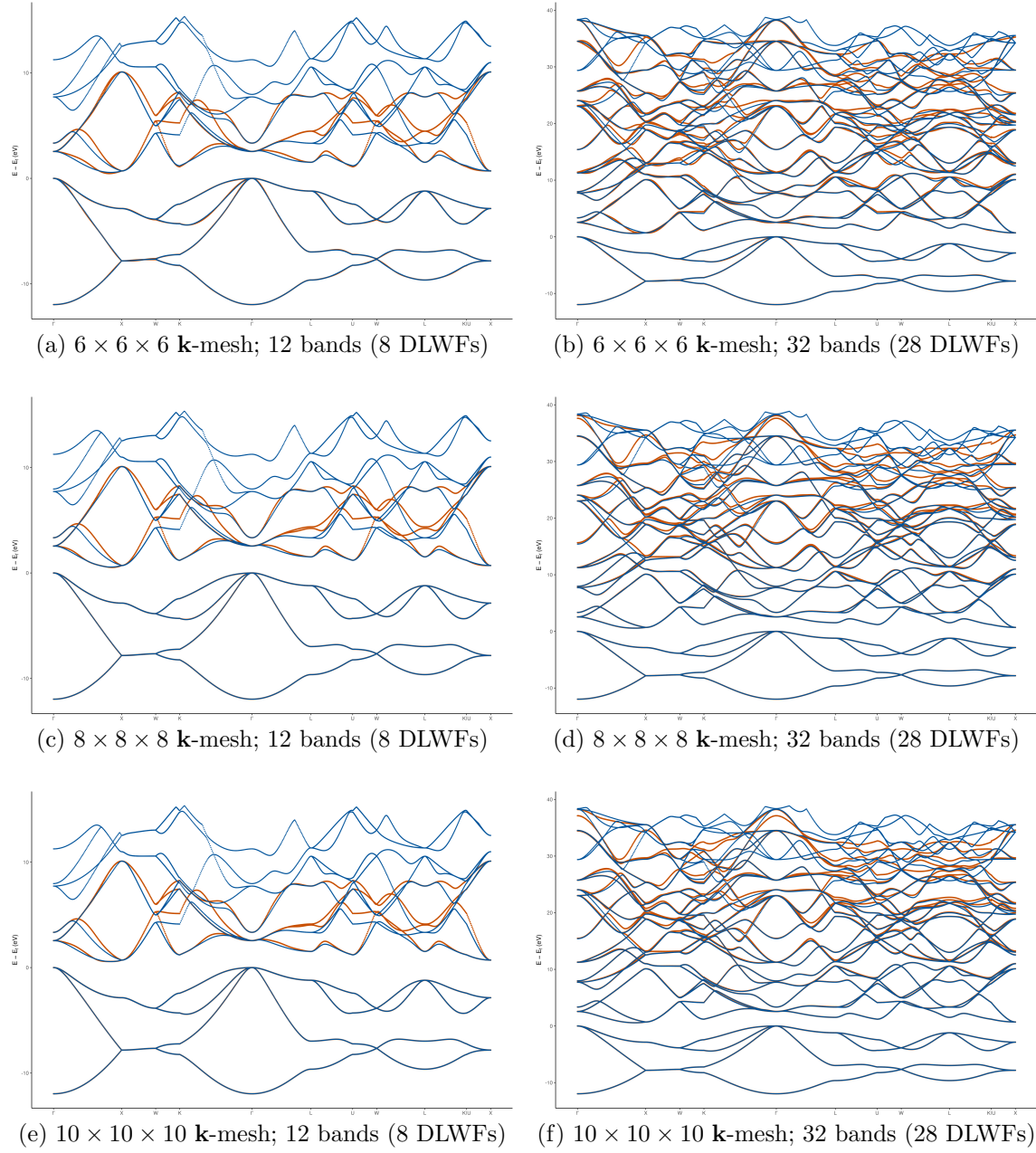


FIG. 5. Band structure of silicon computed from the DFA (blue) and interpolated from the DLWFs (orange). The valence band maximum is set to zero. Subfigures have different Monkhorst–Pack samplings of the Brillouin zone and different numbers  $N_b$  of bands from which the  $N_w$  DLWFs are constructed ( $N_w = N_b - 4$ ).

## V. MIXING PARAMETER CONVERSION

In the molecular formulation of the localized orbital scaling correction (LOSC) method [1], the cost function is given as

$$F = (1 - \gamma')\Omega + \gamma'C'\Xi, \quad (10)$$

where  $\Omega$  is the spatial variance cost and  $\Xi$  is the energy variance cost. We write  $\gamma'$  to differentiate from the mixing parameter  $\gamma$  used in the main text. The constant  $C'$  is added because in atomic units there is a large order of magnitude difference between typical space and energy spreads. This results in mixing parameters that are very close to 1.0, which are difficult to optimize. To keep the space and energy cost within the same order of magnitude, the factor of  $C$  was set to  $1000 a_0^2/E_h^2$  (where  $a_0$  is the Bohr radius and  $E_h$  is one hartree). The implementation in `wannier90` uses the units of Å and eV, which results in spreads that are of the same order of magnitude; thus, we use a factor of  $C = 1 \text{ Å}^2/\text{eV}^2$  in our implementation of the cost function. Converting between these two different equations and units can be accomplished with the following formulae. When converting from Eq. (10), the equivalent mixing parameter for the cost function in the main text is given by

$$\gamma = \left( 1 + \left( \frac{1 - \gamma'}{\gamma'} \right) m^2 C' \right)^{-1} \quad (11)$$

where  $m = 0.529177210903/27.211386245988$  is the conversion from  $a_0$  to Å divided by that from  $E_h$  to eV. Values are obtained from the NIST CODATA database [2]. The conversion from the mixing parameter in the main text to the cost function in Eq. (10) is given by

$$\gamma' = \left( 1 + \left( \frac{1 - \gamma}{\gamma m^2 C'} \right) \right)^{-1}. \quad (12)$$

## VI. CODE IMPLEMENTATION DETAILS

The cost function outlined in the main text was implemented in the `wannier90` code [3–5]. To implement the energy localization, the data structures necessary for energy localization are only calculated if energy localization is requested. The energy spread cost is calculated in the function `wann_xi`, which is called right after the function `wann_omega`, which calculates the spatial spread. Similarly, the energy gradient is only calculated when

needed and is calculated in `wann_dxi`, which is called right after the function that calculates the spatial spread gradient, `wann_omega`. The analytic gradient implemented in `wann_xi` was verified numerically for some test systems to ensure the derivation is correct. The additional data structures that hold the pertinent information for energy localization are `have` for average energy, `have2` for average energy squared, and `h2ave` for average of the squared energy. These variables are used to update the public variables `wannier_energies` and `wannier_espreads`, which are the energy version of the public variables `wannier_centres` and `wannier_spreads` used for spatial information. Since adding these variables into the library mode would necessitate a change to the API, this change was not implemented. If desired, these variables could be added to the API as optional arguments, which should prevent breaking any existing code that uses the API. Our modified code is hosted on GitHub at [6].

#### A. Keyword List

The `wannier90` program uses an input file named `seedname.win`, where `seedname` can be set from the command line. This input file contains key-value pairs in a free-form structure that controls the settings of the program. This is a list of the new keywords added in the implementation of energy localization in the `wannier90` code.

Keyword	Type	Description
Energy Mixing Parameters		
SP_EN_MIX	R	Space and energy mixing parameter
ECONV_MAX	R	Energy convergence maximum
NCONV_MAX	I	Number of WFs to use for convergence
NUM_OCC	I	Bloch orbital occupation per k-point
WRITE_INFO	L	Write localization information per WF to file
WANNIER_PLOT_DENSITY	L	Plot the WF density

---

TABLE VI: `seedname.win` file keywords controlling the energy localization. Argument types are represented by, I for a integer, R for a real number, and L for a logical value.

## B. Keyword Details

`real :: sp_en_mix`

Space and energy mixing parameter; a value of 0.0 gives the MLWF cost function. This value must obey the inequality  $0.0 \leq \text{sp\_en\_mix} \leq 1.0$ . When  $0.0 < \text{sp\_en\_mix}$  then the per WF information printed at every print cycle will change to include the energy statistics.

The default value is 0.0.

`real :: econv_max`

The upper bound for the energy window used for testing localization convergence. This is useful when considering high-energy unoccupied orbitals since they can be very noisy during the descent. If `econv_max` is set then an additional line will be printed at the end of each print cycle showing the spatial, energy, and total cost of the subset used for convergence. This setting cannot be set if `nconv_max` is set.

No default.

`integer :: nconv_max`

The number of Wannier functions used to test for convergence during the gradient descent in the Wannierisation procedure. Useful for when considering high-energy unoccupied orbitals since they can be too noisy to converge during the descent. If `nconv_max` is set then an additional line will be printed at the end of each print cycle showing the spatial, energy, and total cost of the subset used for convergence. This setting cannot be set if `econv_max` is set.

No default, but if `nconv_max > num_wann` it will be set to `num_wann`.



`integer :: num_occ`

The number of occupied of Bloch orbitals. This is used to print the occupation of the WFs. Since it is only a single integer this implementation only applies correctly for insulators and  $\Gamma$ -point calculations. In the typical case of finding MLWFs for occupied only orbitals the WF occupations will always be 1.0. Setting `num_occ` is useful when considering WFs that include both occupied and unoccupied Bloch orbitals.

No default.

`logical :: write_info`

If `true`, write a summary of the cost information per WF to the file `seedname.info` for the WFs in the home unit cell. The format is WF index, Cartesian expectation of center in Å, spatial spread in Å<sup>2</sup>. If `sp_en_mix`  $\neq$  0.0 then it will additionally print the WF energy expectation in eV and the energy spread in eV<sup>2</sup>. If `num_occ`  $\neq$  0 then it will also print the WF occupations.

The default value is `false`.

`logical :: wannier_plot_density`

Plot the WF density instead of the wavefunction, where the density is defined as  $|w_n(\mathbf{r})|^2$ . In the case of WFs that are not strictly real-valued, plotting the wavefunction will truncate the imaginary part. Plotting the density instead guarantees the whole WF is plotted.

The default value is `false`.

- 
- [1] N. Q. Su, A. Mahler, and W. Yang, Preserving Symmetry and Degeneracy in the Localized Orbital Scaling Correction Approach, *J. Phys. Chem. Lett.* **11**, 1528 (2020).
  - [2] E. Tiesinga, P. J. Mohr, D. B. Newell, and B. N. Taylor, The 2018 CODATA Recommended Values of the Fundamental Physical Constants, <https://physics.nist.gov/cuu/Constants/index.html> (2020).
  - [3] A. A. Mostofi, J. R. Yates, Y.-S. Lee, I. Souza, D. Vanderbilt, and N. Marzari, Wannier90: A

- tool for obtaining maximally-localised Wannier functions, *Computer Physics Communications* **178**, 685 (2008).
- [4] A. A. Mostofi, J. R. Yates, G. Pizzi, Y.-S. Lee, I. Souza, D. Vanderbilt, and N. Marzari, An updated version of wannier90: A tool for obtaining maximally-localised Wannier functions, *Computer Physics Communications* **185**, 2309 (2014).
- [5] G. Pizzi, V. Vitale, R. Arita, S. Blügel, F. Freimuth, G. Géranton, M. Gibertini, D. Gresch, C. Johnson, T. Koretsune, J. Ibañez-Azpiroz, H. Lee, J.-M. Lihm, D. Marchand, A. Marrazzo, Y. Mokrousov, J. I. Mustafa, Y. Nohara, Y. Nomura, L. Paulatto, S. Poncé, T. Ponweiser, J. Qiao, F. Thöle, S. S. Tsirkin, M. Wierzbowska, N. Marzari, D. Vanderbilt, I. Souza, A. A. Mostofi, and J. R. Yates, Wannier90 as a community code: New features and applications, *J. Phys.: Condens. Matter* **32**, 165902 (2020).
- [6] A. Mahler, Mtesseract/wannier90: CostSE, <https://github.com/mtesseract/wannier90> (2024).